# Investigating spatio-temporal deformation in single crystal Ni-based superalloys using *in-situ* diffraction experiments and modelling

Ayan Bhowmik*[1], Junyi Lee[2], Suki Adande[1], Ming Wang Koh[3], Tea-Sung Jun[1], Giorgio Sernicola[1], T. Ben Britton[1], Catherine M.F. Rae[3], Daniel Balint[2], Finn Giuliani[1,2]

[1]*Department of Materials, Imperial College London, London SW7 2AZ, UK*
[2]*Department of Mechanical Engineering, Imperial College London, London SW7 2AZ, UK*
[3]*Department of Materials Science and Metallurgy, University of Cambridge, Cambridge CB3 0FS, UK*

*Abstract*

In this study, we perform a detailed analysis of the room temperature deformation of a [100]–orientated single crystal Ni-based superalloy, CMSX-4 micropillar, using a combinatorial and complimentary characterisation approach of micro-Laue diffraction coupled with post-deformation microscopy and crystal plasticity modelling. Time-resolved micro-Laue data indicated that deformation initiated by activation of multiple slip (after 5% engineering strain) which led to the generation of a plastic strain accumulation accompanied by a two-fold increase in the dislocation density within the micropillar. Subsequent to that, slip occurred primarily on two systems $(1\bar{1}1)[101]$ and $(111)[\bar{1}01]$ with the highest Schmid factor in the single crystal micropillar thereby resulting in little accumulation of unpaired GNDs during a major part of the loading cycle, upto 20% strain in this case. Finite element crystal plasticity modelling also showed good agreement with the experimental analyses, whereby significant strains were found to develop in the above slip systems with a localisation near the centre of the micropillar. Post-deformation transmission electron microscopy study confirmed that deformation was mediated through a/2<110> dislocations on {111} planes in the γ-phase, while high stress levels led to shearing of the γ′ precipitates by a/2<110> partials bounding an anti-phase boundary free to glide on the {111} planes. During the deformation of the single crystal micropillar, independent rotations of the γ and γ′ phases were quantified by spatially resolved post-deformation micro-Laue patterns. The degree of lattice rotation in the γ-phase was higher than that in the γ′-phase.

**Keywords**: Micro-Laue diffraction, CMSX-4, single crystal superalloys, micropillar compression, crystal plasticity, slip system

* *Corresponding author: Email: ayan99@gmail.com*

## 1. Introduction

Single crystal Ni-based superalloys have been singularly used in the hottest parts of the jet engine viz the turbine section, particularly blades. These alloys contain two major phases – (i) a face centred cubic (A1) Ni-base solid solution (γ-phase), present as channels and (ii) $L1_2$ ordered $Ni_3Al$ precipitates (γ′-phase) with cuboidal morphology [1]. The ordered γ′-phase acts as strengthening constituent, which renders exceptional strength to the superalloys at high temperatures. The major difference between these two phases arises from the fact that the Burgers vector of the main gliding dislocation (a/2<101>) in the γ-phase is half that of the so-called 'super dislocation' (a<101>) in γ′-phase. Hence, as consequence of slip transfer across the γ/γ′-boundary, the a<101> dislocation creates an anti-phase boundary (APB) by splitting into partials [1–4]. This splitting mechanism can happen on both the {111} and {010} planes in γ′, thereby creating the so-called 'Kear-Wilsdorf' (KW) locks, particularly at high temperatures when the mobility of the partials are high on both these sets of planes. This mechanism is behind the phenomenon of yield strength anomaly of γ′ and hence Ni-based superalloys at elevated temperatures up to 800˚C [1,5,6].

*In-situ* micropillar compression is an effective and versatile technique to understand the inherent stress-response of materials through controlled deformation within well-defined material volume upon application of load, enabling direct measurement of the load-response behaviour of the material and concurrent correlation with associated microstructural changes [7–16]. In recent years, the scope of this method has widened beyond simply measuring the intrinsic mechanical properties of single-phase materials to being applied directly in understanding deformation behaviour of two-phase engineering alloys. In transformation induced plasticity (TRIP) steel, though micropillar compression, the mechanism of transformation of austenite to ε and α'-martensite through dislocation pile-ups and shear strain accumulation, has been observed directly [17,18]. Using GaN micropillars, plastic parameters such strain-rate sensitivity and activation volume could be directly quantified [16]. In a precipitation-hardened Mg-5%Zn alloy, direct measurement of stresses for different deformation-mediated processes, such as twinning and precipitate shearing, depending on the pillar orientation, could be obtained [19]; pillars oriented for basal slip activation showed direct microstructural

evidence of precipitate shearing. In two-phase Zircaloy-4, containing a Zr-rich matrix phase and a ZrH phase, compression of micropillars coupled with TEM and micro-Laue observations showed direct evidence of shear bands initiating in the matrix phase and terminate at hydride packets. However, by changing the orientation of the micropillar, deformation within hydride packets was mediated through formation of twins and dislocations [20]. Using micropillar compression, a distinct size-effect on the deformation mechanisms in precipitation-hardened duralumin and high entropy alloys has also been ascertained [21,22]. Micropillar experiments with α/β Ti alloy showed that the morphology of the second phase (β) is a determining factor in the deformation of two-phase alloys and that local slip predicted by Schmid law become ineffective when the arrangement of the β-phase changes significantly [23]. Also, by conducting controlled micropillar compression experiments in a bcc *β* Ti-alloy (Ti-Fe-Mo based) with aged B2 TiFe precipitates, significant hardening in the alloys could be conclusively attributed to the fine B2 precipitates resisting dislocation cutting [24].

Furthermore, with the development of *in-situ* diffraction techniques, such small-scale mechanical tests can be performed in a dynamic mode. Particularly noteworthy is the application of micro-Laue diffraction in understanding the material deformation in three-dimensions under various test conditions. Using a focused sub-micron sized beam, micro-Laue diffraction provides information from the entire volume of the micropillar and not just surface, and the use of a "white" beam enables probing the evolution of rotational and strain gradients in both polycrystals [15,25] and single crystals [8,26–29]. *In-situ* micro-Laue diffraction has been used to study detailed material response under various forms of loading such as tensile [30], micropillar compression [10,11,20,26,28], bending [12] and nano-indentation [27]. During plastic deformation, changes in the crystal orientation, strain gradients and polygonisation within the illuminated volume resulting from activation of particular slip plane and rearrangement of dislocations to minimizing strain energy is manifested either as streaking or splitting of the Laue peaks [14,31,32].

Past studies on single crystal micropillar of superalloys have particularly focused on studying the fundamental size dependent plasticity effects [33–35]. One of the papers that dealt with size effects on superalloys was by Uchic et al. [35] where a

transition from bulk-like to size-affected behaviour was observed for samples with ~5 μm diameter and smaller. Following that work, Shade et al.'s [33] work demonstrated the differences in flow behaviour in Ni-based superalloy (René-5) microcrystals between the dendritic and interdendritic zones. Again, with 5 μm diameter pillars they found a mean-field type behaviour for all their pillars. However, Arora et al. [34] carried out size effects studies on CMSX-4 and found explicitly that for micropillar dimensions <2.0 μm, the "smaller is stronger" principle holds true but sizes >2.0 μm, the yield strength of the micropillars is independent of size. However, Arora et al. carried out post-mortem analyses of their micropillars using SEM that could only provide limited information about the slip activities; they particularly saw the activation of multiple {111}-type planes as deduced from slip traces. Neither did they had the means to study the dynamic evolution of plastic strain within the pillar nor relate the findings with post-mortem microscopy.

But with the recent development of *in-situ* white light based micro-Laue diffraction, the temporal and spatial evolution of deformation within a deforming small volume, *e.g.* within a micropillar, can be characterized using a micro-focused beam. Here we have applied this technique to study the uniaxial deformation behavior of [100]-oriented single crystal Ni-based superalloy CMSX-4. We envisaged this technique would help to interpret the performance of individual microstructural features in the single crystal in a dynamic mode and provide useful insights into the evolution of the deformation structure. Through time-resolved data analysis, a direct connection between applied strain and formation of microstructural defects such as shear band nucleation, dislocation multiplication, dislocation shearing γ′ precipitates *etc.*, could be established. This is otherwise impossible in case of conventional testing procedures where only the final microstructure with its defects are characterised and studied. Further, post-deformation transmission electron microscopy studies have been conducted to corroborate and complement the findings from micro-Laue diffraction experiments during micropillar loading. The deformation behavior of the micropillar, as observed experimentally, has also validated with crystal plasticity modeling of the micropillar compression.

## 2. Experiment and crystal plasticity modeling

### 2.1. Experimental procedure

A single crystal specimen of CMSX-4, fabricated by conventional investment casting route, was used for the study. The cast specimen was homogenised, subjected to heat treatment and ageing: primary heat treatment of 2 hours at 1140°C and ageing for 16 hours at 870°C were performed. A rectangular block of the specimen was sectioned and subsequently mechanically polished to a thin slice of ~200 μm thickness. Cylindrical micropillars of dimension 4 μm (diameter) × 7 μm (height) were then milled on the thin edge of the slice, with the pillar axis parallel to the [100]-direction, using focused ion beam (FIB) on a Helios NanoLab 600 scanning electron microscope (SEM). We selected the size of our pillar such that the load response is not dominated strongly by the pillar length scale but rather gives an indication of the bulk behaviour of the Ni-based single crystal [34]. An accelerating voltage of 30 kV and polishing currents down to 90 pA were used for pillar fabrication. Significant volumes of material around the pillars were also milled out in order to eliminate or minimize the interaction of the x-ray beam with surrounding material. The actual micropillar axis was determined to be parallel to [9.95, 0.96, 0.23] which is ~5.7° deviated from the [100] crystal direction.

*In-situ* micro-Laue diffraction and micropillar compressions were carried out on 34-ID-E beam line at the Advanced Photon Source, Argonne National Laboratory, USA. A schematic of the experimental set-up is shown in Figure 1. A white 7-30keV x-ray beam was passed through a Si (111) monochromator and focused to a probe size of 0.4 μm × 0.4 μm using a pair of horizontal and vertical focusing Kirkpatrick-Baez (KB) mirrors. The sample stage was inclined at an angle of 45˚ to the incident beam and experiment was performed in the reflection mode. The diffraction patterns from the sample were captured following the test using a 409.6 mm × 409.6 mm amorphous Si-CCD area detector (2048 × 2048 pixels) (Perkin Elmer). At first, the diffracted peak profile from annealed Si wafer was studied in order to check the beam spread caused by the instrument and detector alignment. Following compression, the micropillar was scanned along the longitudinal axis with a step of 1 μm and exposure time of 4s. The samples were compressed on an Alemnis displacement controlled indenter at room temperature using a flat diamond punch with an engineering strain rate of $10^{-4}s^{-1}$ and unloading strain rate of $10^{-2}s^{-1}$. Due to the presence of crystallographically oriented γ and γ′ phases in CMSX-4, the Laue pattern shows two closely associated spots at every position on the CCD camera.

Post-deformation micrographs of the compressed pillars were obtained using the Helios SEM. Further, the deformed pillar was sectioned using FIB and electron-transparent foils were lifted-out. The microstructure of the cross-section foil was studied using a JEOL 2100F transmission electron microscope (TEM). The pillars were investigated using conventional bright and dark field imaging modes and also by obtaining appropriate selected area electron diffraction (SAED) patterns.

### 2.2. Finite element crystal plasticity model

Crystal plasitiicy models consider the individual slips systems and dislocations to model the deformation of a material, which allows mechanisms such as the KW locks to be studied. Therefore, a crystal plasticity finite element (CPFE) model was constructed in order to study the deformation behaviour of the CMSX-4 micropillar. The finite element model and the relevant boundary conditions are shown in Figure 2. In this study, the dimensions of the pillar in the simulations are identical to that of the experiments and the indenter punch is displaced based on the speed of the punch in the experiments. As in the experiment, the orientation of the crystal (x-axis) in the micropillar in the finite element model is applied to be parallel to [9.95, 0.96, 0.23] direction. A friction coefficient of 0.15 was applied between the indenter and the micropillar.

The crystal plasticity material model is implemented in a commercial finite element software, Abaqus, *via* a custom UMAT subroutine. The punch is an analytical rigid surface and the micropillar is made from hexahedral elements (C3D8) with a total of 213729 nodes and 203486 elements. The micropillar is made from two phases, $\gamma$ and $\gamma'$, which constitute the channels and precipitates respectively. Therefore, the individual phases are assigned different material properties in the finite element analysis, and the channels and precipitates are assigned as shown in Figure 2, where the micropillars are made up from mostly cubic precipitates (with lengths of 0.3 μm) and channels (that are 0.05 μm thick).

In this work, the CPFE model by Asaro [36,37] is used to model the material with the precipitates and channels having different material properties that reflect their mechanical behaviour. This approach is selected over more advanced models, such as the one proposed by Keshavarz et al. [38,39] which is more accurate, because of the difficulty of implementing the model on the micro-pillar simulations as the simulations using that model did not converge and significant changes to the finite

simulation calculations are required. Nonetheless, the current CPFE model can provide some insights and help explain several observations made in the experiments qualitatively.

The stress-strain behaviour of the material can be described by the following equation.

$$\dot{\sigma}_{ij} = C_{ijkl} D^E_{kl} + \omega_{im}\sigma_{mj} - \sigma_{im}\omega_{mj} \quad \text{Eq. (1)}$$

Where $\sigma_{mj}$ is the stress, $\dot{\sigma}_{ij}$ is the rate of increase in stress, $C_{ijkl}$ is the elastic tensor, and $D^E_{kl}$ and $\omega_{mj}$ are the elastic stretch and spin tensors, which are calculated from the deformation gradient, $F_{ij}$, as follows.

$$F_{ij} = F^E_{im} F^P_{mj} \quad \text{Eq. (2)}$$

$$L^P_{ij} = \dot{F}^P_{im}\, F^{-P}_{mj} = \sum_{\alpha} \dot{\gamma}^{\alpha}\, s^{\alpha}_i n^{\alpha}_j \quad \text{Eq. (3)}$$

$$D^E_{kl} = \frac{1}{2}(L^E_{ij} + L^E_{ji}) \quad \text{Eq. (4)}$$

$$\omega^E_{kl} = \frac{1}{2}(L^E_{ij} - L^E_{ji}) \quad \text{Eq. (5)}$$

$$\tau^{\alpha} = s_i \sigma_{ij} n_j \quad \text{Eq. (6)}$$

where the superscripts $E$ and $P$, denote elastic and plastic deformation, respectively, $L_{ij}$ is the velocity gradient, $\dot{\gamma}^{\alpha}$ is the slip rate, $s_i$ the normalised vector of the slip direction, $n_j$ is the normalised vector of the normal of the slip plane, $\tau$ is the resolved shear stress, and the superscript $\alpha$ denotes the slip system.

$$\dot{\gamma}^{\alpha} = \dot{a} \cdot sgn(\tau^{\alpha}) \left( \left| \frac{\tau^{\alpha}}{g^{\alpha}} \right| \right)^{n} \quad \text{Eq. (7)}$$

$$\dot{g}^{\alpha} = \sum_{\beta} h_{\alpha\beta} \dot{\gamma}^{\beta} \quad \text{Eq. (8)}$$

$$\dot{\sigma}_{ij} = C_{ijkl}\left(\dot{\varepsilon}_{kl} - \dot{\varepsilon}^{p}_{kl}\right) = C_{ijkl}\left( \dot{\varepsilon}_{kl} - \sum_{\alpha} \frac{1}{2} \dot{\gamma}^{\alpha} (s^{\alpha}_k m^{\alpha}_l + s^{\alpha}_l m^{\alpha}_k) \right) \quad \text{Eq. (9)}$$

where $\tau$ is the resolved shear stress, $m_i$ and $s_j$ are the slip plane normal and slip direction respectively, $g$ the slip system hardness, $\gamma$ is the plastic shear strain, $\dot{a}$ and $n$ are material parameters, $h$ is the slip plane hardening moduli, $\sigma$ is the stress, $\varepsilon$ is the strain, and $C$ the fourth-order stiffness tensor. The subscripts and superscripts $\alpha$ and $\beta$

denote the $\alpha$-th and $\beta$-th slip systems respectively. The number of slip systems and their orientations depend on the crystal lattice structure. Lastly, the superscript $p$ denotes plastic strain and the dot above the variable denotes the time derivative of the variable.

The hardening laws that describes the values of $h_{\alpha\beta}$ are as follows [37,40].

$$h_{\alpha\beta} = \begin{Bmatrix} h(\gamma) = h_0 \operatorname{sech}^2 \left|\frac{h_0 \gamma}{\tau_s - \tau_0}\right| & , \alpha = \beta \\ q h(\gamma) & , \alpha \neq \beta \end{Bmatrix} \quad \text{Eq. (10)}$$

$$\gamma = \sum_{\alpha=1}^{n} |\gamma^{\alpha}| \quad \text{Eq. (11)}$$

where $h_{\alpha\alpha}$ and $h_{\alpha\beta}$ are the self and latent hardening moduli, $h_0$ is the initial hardening gradient, $\tau_0$ in the initial critical resolved shear stress, $\tau_s$ is the saturated critical resolved shear stress, and $q$ is the hardening factor.

The crystal plasticity material model is implemented in commercial finite element software, Abaqus, *via* a modified UMAT subroutine [40]. The material properties used in this study is based on a study performed in [41] and they are summarised in Table 1.

Both the $\gamma$ and $\gamma'$ phases are FCC crystals, but in order to simulate the different behaviours of the different phases the critical resolved shear stress, $\tau$, of the precipitates are set to be twice the value of the channels. As in the experiment, the orientation of the crystal (x-axis) in the micropillar in the finite element model is input to be [9.95, 0.96, 0.23] direction.

## 3. Results and discussion

### 3.1. Load response of CMSX-4 micropillar

A load-displacement curve of the [100]-CMSX-4 pillar following compression in the beamline is shown in Figure 3(a). The micropillar samples were compressed by 2 μm, which correspond to an actual uniaxial strain of ~20% (28% for uncorrected raw data). Following an elastic loading, a clear drop in stress of ~150 MPa was observed, and then the material is seen to work harden steadily. Following a set displacement of 2 μm of the indenter head with a displacement rate of 0.7 nm $s^{-1}$, the punch was retracted at a rate twice that of loading. During evaluation of materials'

properties through such *in-situ* loading experiments, it is important to consider the role of the compliance of the loading stage which includes stiffness of the adhesive (used to stick the sample to SEM stub) and load frame [42]. For this, a separate experiment with a pillar fabricated from the same sample was tested and corrected for compliance. The details of the method are described in the Appendix. From the corrected curve, the room temperature yield strength of [100]-CMSX-4 is noted to be ~1.2 GPa – this is in agreement with bulk yield stress previously reported for CMSX-4 at room temperature [43]. A similar treatment was given to the load-displacement data obtained for the micropillar tested in the beamline and the compliance-corrected engineering stress-strain curve obtained by the method is shown in the inset of Figure 3(a).

Figure 3(b) shows the SEM image of the micropillar after deformation in the beamline. The figure shows the appearance of slip lines on the walls of the pillar. The slip traces are found to lie along the {111} planes, obtained by measuring the glide angle, having the highest Schmid factor for the given pillar orientation. This is expected in the A1-$L1_2$ aggregate, where slip occurs on the {111} plane through glide of ribbons of a/2<101> dislocations in the A1 phase. A careful investigation indicated that the slip did not continue to form a glide step and the micropillar also showed evidence of significant bulging on both sides.

### 3.2. *In-situ* micro-Laue diffraction study

#### *3.2.1. Laue patterns from the parent micropillar*

Firstly, two peaks, 035 and $\bar{1}57$, from the annealed stress-relieved Si-wafer standard sample, are shown in Figure 4(a and b), where the peaks have a smooth and symmetrical profile. Sections from the three-dimensional profile of the peaks are also shown in Figure 4(c and d) respectively. The full-width-at-half-maximum (FWHM) of the peaks is calculated to be 0.08˚ – this can be considered as a contribution from instrumental broadening. Thus, any additional broadening must result from the presence of internal deformation gradient and hence the GND density within the test specimen. Using the Cahn–Nye relationship, the GND density in the pillar can be obtained from $\rho = |\kappa|/b$, where $b$ is the magnitude of the Burgers vector and $\kappa$ is the local lattice curvature. In this model, the whole pillar is divided into coherent cells of size $\Delta s$ and the pillar is assumed to be composed of equal number of dislocations with

opposite signs with a dislocation in each cell. The lattice curvature is given by $|\kappa| = \Delta\theta/\Delta s$, $\Delta\theta$ is the orientation spread. Now we consider the micropillar domain size to be uniform along the penetration depth of the beam in the pillar, which is given by D, the width of the incident beam (= 400 nm). By substituting the white light broadening resolution $\Delta\theta = 0.08^\circ = 1.4\times10^{-3}$ radians, the average Burgers vector of 0.2537 nm, taken as an average of the a/2<101> dislocations in the γ and γ′ phases, the minimum detectable GND density in the CMSX-4 micropillar is therefore $2.7\times10^{12}$ $m^{-2.}$

Figure 5(a) shows the $\bar{1}19$ peak obtained from the parent micropillar sample. Supplementary Figure S1 also shows various Laue peaks, isolated from the main pattern. As already mentioned in the previous section and seen from the peaks, two closely associated peaks are always distinctly associated with any reflection from the alloy. By carrying out an energy scan over a narrow energy band of 15.3±0.3 keV (with a step of 0.003 keV) corresponding to the excitation of the $\bar{1}15$ peak, the integrated intensity *vs* diffraction vector, Q (= $4\pi sin\theta/\lambda$) can be plotted. From the plot, it can be ascertained that twin peaks belong to the γ and γ′ phases (Figure 5(b)). Owing to a higher volume fraction and higher degree of structural ordering, the γ′-$Ni_3Al$ peak has a higher intensity than the γ phase [44]. The angular difference between the twin peaks is ~0.45°, which gives an estimate of the angular misorientation, about the beam direction, between the two phases in the single crystal. Such minor angular misorientation between the two (γ and γ′) phases in single crystal superalloys has been recently reported in an experimental single crystal superalloy following different heat-treated conditions [45]. The generation of lattice misorientation in single crystal superalloy has not only been observed between dendrites, dendritic and inter-dendritic region [46] but also at the γ/γ′-interface level following heat treatment. Using neutron diffraction, Wu et al. [45] reported an average misorientation of ≤ 0.9° at the γ/γ′-interface and our observed misorientation value lies well within this range. This angular distortion is caused by the existence of local shear stresses around the γ′-phase. At room temperature, with larger γ lattice parameter (0.3589 nm) than γ′ (0.3587 nm), CMSX-4 has a negative lattice misfit of magnitude $0.6782\times10^{-3}$ [47]. Besides, interfacial dislocations to account for the lattice misfit, additional dislocations within the matrix would also be expected to accommodate this angular distortion between the phases. Using measured

misorientation, θ = 0.45˚, between the two spots and relating this to the lattice curvature between the two phases, the GND density, ρ, corresponding to the mismatch can be estimated using the relations $^{b}/_{h} = 2\sin\theta$ and $\rho = {}^{1}/_{Dh}$. It is assumed that slip occurs on single system, *i.e.* octahedral slip, in the γ and also γ′ wherein no slip of the a/2<101> partials is considered to take place on the {010} plane in the latter phase; also formation of complex superlattice stacking faults involving complicated dislocation reactions is ignored and only APB formation, with the lowest energy of formation, is considered. Hence, using an average Burgers vector, $b$=0.2537 nm of the γ and γ′ phases and probed area, $D$ = 4 μm, the estimated GND density is $2.05\times10^{14}$ $m^{-2}$. Another feature of the peaks is that it shows an FWHM of 0.3˚, which is much higher compared to the Si standard peaks. This clearly implies the presence of a residual strain already within the parent micropillar sample. This can be either due to the presence of excess unpaired dislocations (*i.e.* GNDs) in the sample or due to Ga-irradiation damage of the pillar. It has been seen that this Ga-impregnated damaged, amorphous layer forms a hardened skin, which leads to a prior strain gradient in metallic micropillars [9,48,49]. A fraction of the strain could also be accounted to the coherency strain between the γ/γ′ phases although the deconvolution of the total strain into components is yet to be understood from the micro-Laue data. From the calculations presented above the parent sample already had a significant dislocation density prior to compression and the contribution of this to the streaking of the spot cannot be discounted. However, TEM observation of the pillar morphology and microstructure presented later would help understand the cause of streaking better.

### *3.2.2. Time-resolved Laue pattern during deformation*

During the compression experiment, in order to track the progress of deformation the sub-micron sized white beam was probed at a point ~3.5 μm from the top of the micropillar with 4s exposure time per frame. Figure 6(a-d) shows the evolution of the $\bar{1}19$ peak with the applied strain from that corresponding to post-yielding of the micropillar up to peak load and then after complete unloading. In order to give an indication of the change in the peak intensity, shape and streaking, the residual intensity distribution from each frame was obtained by subtracting the initial frame from the respective frames, and the maps are shown in Figure 6(e-g). The evolution

of four other peaks with the strain isolated from the main pattern is also shown in Supplementary Figure S2 (a-d) along with the respective residual maps. Interestingly, very little movement in the diffraction spots was obtained from the particular beam position on the pillar during loading through peak load and until unloading. No movement of the diffraction spots was observed during the compression experiment when the *in-situ* diffraction patterns were being obtained; this crucially implies that no bending of the micropillar occurred under loading – this would mean that the applied strain went towards actual compression of the sample [26,27]. As can be seen from the residual sequence of the peaks, there is only a slight increase in the streaking of the γ′ peak at ~5% strain (compliance corrected strain corresponding to a load of 25.4 mN) with the streaking remaining constant up to the peak load. However, no discernible residue in the γ-peak could be observed. Streaking of Laue peaks is assigned, in general, to the presence of lattice strain caused by the persistent slip generating an excess number of unpaired GNDs on a given slip system [14,31,50]. It has been previously observed that during compression of pure Cu single crystal micropillars, the diffraction peak width and shape stayed nearly constant up to an engineering strain of 18%, when the pillar is perfectly aligned under the indenter punch [51]. In this case, there was no storage or build-up of GNDs on the preferred slip system with geometrically the highest Schmid factor. However, it was suggested that when the micropillar was misaligned with respect to the punch, considerable streaking was observed due to excess dislocations being multiplied and stored on slip system with a lower Schmid factor until the misalignment is finally accommodated [51]. In the present experiment, a small increase in streaking of the γ′ peak was observed at the early phase (up to 10%) – this suggests that there had been some accumulation of GNDs on slip system with lower geometrical Schmid factor during the early phase of plastic deformation. However, following this, until a strain of ~20% (compliance corrected strain) *i.e.* up to peak load, only a very little change the peak width or shape is noticed indicating that the dislocations (a/2<101>) are essentially generated on the {111} plane with the highest Schmid factor. As Table 2 shows two slip systems have the highest Schmid factors for the given loading axis, *i.e.* $(11\bar{1})[101]$ and $(111)[\bar{1}01]$, considering the single crystal micropillar as one coherent unit. Thus, with no misalignment of the micropillar with respect to the indenter punch, the strain is accommodated by these two slip systems both in the A1-γ and $L1_2$-γ′ phases with smooth glide of dislocations on the slip planes without the

development of strain due to dislocation build-up that might have been the case otherwise had a lower Schmid factor slip system been operative. It is to be noted that for the given orientation of the micropillar, the $(1\bar{1}1)[110]$, $(111)[\bar{1}10]$ and $(\bar{1}11)[110]$ slip systems have very close Schmid factors. Thus, it is not unfeasible that slip might have initiated on these slip systems first and later transitioned to the two systems with the highest factors and thereby causing streaking of the spots during the early stages of compression. The Laue peak after unloading still showed a remnant streaking relative to the initial frame. This implies the presence of a remnant plastic strain within the micropillar. This would be manifested in the form of excess unpaired GNDs in the sample as compared to the parent sample.

Owing to its industrial significance as high temperature material, in the past, detailed microstructural characterisation of the single crystal superalloys have been carried out using microscopy, both SEM and TEM. To understand the basic deformation behaviour of such alloys, room temperature tensile and compressive tests have been carried out and the resultant deformation structure investigated [52–54]. However, the limitation of post-deformation identification of either slip bands (generally carried out by slip trace analyses on the deformed sample surface in SEM) or detailed analyses of dislocation structure and reactions (performed by TEM) give a final representation of the microstructure resultant after a certain degree of deformation and induced strain instead of a dynamic correlation between strain distribution and simultaneous microstructural evolution. Analyses of slip lines on the surface of uniaxial test specimens firstly cannot exactly provide conclusive inference on the interactions between dislocations and the coherent precipitates and secondly in a bulk sample more often the microstructural discontinuities such as pores and eutectic pools influence the evolution of plastic localisation [52]. Using in-situ synchrotron x-ray imaging the growth structure of dendrites and related segregation in single crystal superalloys, fatigue crack propagation paths have been studied recently with time [55,56]. Another method of using monochromatic synchrotron radiation with micron size spot size have been studied on real time turbine blades where the lattice parameters of the phases were probed and the state of internal stress within the turbine blade could be determined [46,57]. However, the probe size used in such experiments was of the orders of few microns in comparison to the submicron beam size used in the present experiments, wherein microscopic deformation mechanisms, such as plastic slip on preferred crystallographic planes, slip transfer, accumulation of

geometrically necessary dislocations (GND) at areas of strain localisation *etc.*, could be studied at a finer scale. Owing to the application of white light, resultant changes in lattice parameters due to strain gradient in the sample allows the diffracted beams to be in prominence and track the resultant changes in its shape and position. Most of such monochromatic synchrotron based work [58–60] use lattice parameter calculations as a means to study their evolution and resulting misfit between γ and γ′ phases during high temperature loading. But the combinatorial and complimentary characterisation approach of micro-Laue diffraction coupled with TEM and crystal plasticity on uniaxial loading allow us to relate the stress response of the material describing the full field plastic strain in three-dimension with the microstructure of the deforming volume [27,61]. From the sequence of time-resolved peak data, it is deduced that strain accommodation by multiple slip systems occurred at rather early stages of straining of the CMSX-4 single crystal but subsequently only the primary slip systems operated until the end of the experiment, in this case. Once the main slip plane dominates, the interface between the matrix and coherent precipitates (γ/γ′ interface) does not create an obstacle to the propagation of the slip band. No marked localization of the slip is observed as a result of the coherent precipitates and also the local flow stress within the slip bands was not greatly reduced by the precipitate cutting processes [62]. Following the initiation of a persistent slip band within the single crystal, the dislocations could easily escape from the free surface resulting in a net near-zero accumulation of dislocations within the micropillar after 5% strain.

### *3.4.3. Post-deformation Laue patterns*

A line scan along the vertical pillar axis of the deformed pillar was carried out to spatially map the state of deformation in the micropillar. Figure 7 shows the diffraction spots obtained from different positions, numbered 1-8, from the top to the base of the deformed pillar, with a final height of ~5 μm, following unloading with a step size of 1 μm; the $\bar{1}19$ spots from these locations in Figure 7(a). Other reflections chosen from the whole Laue pattern at these locations are additionally given in Supplementary Figure S3 (a-d). Examining the series of spots in Figure 7, it is clear that position 1 is outside the pillar and the beam is only incident at the top of the pillar at position 2. The relative weakness and diffused nature of the spots from positions 2 and 3 suggest that the top of the pillar is particularly highly strained. Additionally, given the separation between the scan points being 1 μm, this strained layer is

457 believed to extend up to 1 μm from the top surface – this agrees well with the direct
458 observation of the depth of the strained layer seen on the top of the pillar in dark-field
459 TEM, shown in Supplementary Figure S4. Nevertheless, due to friction and initial
460 imperfect alignment between the flat punch and the pillar top surface, the top edges of
461 the sample generally develop a region of shear stress concentration, which is
462 confirmed both by Laue scans and TEM observation. In position 4, both the peaks are
463 significantly broadened. It can be observed that the γ′ peak has a stronger intensity
464 and greater broadening compared to the γ peak. However, the γ reflection gets
465 stronger and broader near the bottom half of the micropillar, which implies an
466 orientation spread in the γ phase. Also in locations 7 and 8, near the bottom of the
467 pillar, the γ peaks are also seen to streak appreciably indicating a higher accumulation
468 of strain in the A1 phase near the base of the pillar. Also, a satellite peak is seen to
469 develop next to both the γ and γ′ peak, observed from positions 6, 7 and 8. This
470 implies the formation of cells in both γ and γ′ phases resulting from dislocations
471 grouping within boundaries. A possible scheme for the formation of such a subgrain
472 structure is discussed later.
473
474 The two closely associated peaks from γ and γ′ in each frame were fitted
475 subsequently with two 2D-Gaussian functions, and their centres (peak positions) were
476 obtained. An example of the fit is shown in Supplementary Figure S5. The degree of
477 movement of the peak centres would give an indication of the relative rotation of the
478 individual phases about the pillar axis with respect to the top of the pillar. This has
479 been plotted in Figure 7(b) for the γ and γ′ peaks. This analysis has only been
480 performed from positions 2 to 7. Although significant areas from around the
481 micropillar were milled-out by FIB in order to prevent obstruction to the path of the
482 diffracted beam but still some substrate effect on the Laue pattern at the base of the
483 pillar particularly, *i.e.* position 8, could not be completely dismissed. It is observed
484 that the extent of relative rotations of the two peaks is different – the rotation of the γ-
485 phase is larger compared to the γ′. While the γ phase undergoes a relative lattice
486 rotation of 0.2˚, the γ′ only does so by 0.05˚ along the axis of the micropillar during
487 loading. Lattice rotation is common during plastic deformation of constrained volume
488 due to the generation of GNDs [63]. With the micropillar being constrained at the top
489 and bottom, the sample undergoes lattice rotation during deformation [11,28]. The
490 interesting finding here is that the two phases are seen to undergo rotations to

different degrees along the vertical axis of the micropillar. This is captured by the sub-micron size resolution of the incident white x-ray probe – such small, relative rotations between the two phases are extremely difficult to capture in post-deformation transmission electron microscopy, where the bending of the foil due to residual stresses or ion milling damage can easily obscure small misorientations. An interesting extension of this study would be to use micro-Laue diffraction to investigate the deformation behavior of single crystal superalloys at high temperatures when individual γ and γ′ phases show different plasticity and load sharing capacities that can be captured by taking into account the relative shapes and movements of the superlattice reflections. However, optimizing the loading stage and thermal drift of the punch at high temperatures during such dynamic *in-situ* experiments remain a challenge.

### 3.3. Microstructure of sectioned pillar

#### *3.3.1. Cross-section of undeformed micropillar*

Figure 8(a-c) shows the TEM bright field images of the sections lifted-out from undeformed (parent) and deformed micropillars. The parent sample shows a uniform distribution of cuboidal γ′-precipitates over γ-matrix bearing the conventional cube-on-cube orientation relationship. The loading direction, which is [100] can be seen to be parallel to the vertical γ channel. The mean γ′-size was ~0.3 μm. It has also been observed that the parent material was not completely strain-free, which is evident from the dislocations that are already present. The dislocations are evenly spread across both the phases. Given this appreciable density of dislocation, it is believed that the micropillar was obtained from the interdendritic region or even at the transition of dendritic/interdendritic regions since these regions of as-cast superalloy contains more dislocations than the dendrite cores. On the two sides of the pillar, an amorphous skin of thickness nearly 50 nm is also directly observed in the cross-sectioned TEM, shown in Supplementary Figure S6, contributing to the amorphous ring pattern in the corresponding SADP. This is due to radiation damage caused by Ga ion during milling at 30kV ion voltage using FIB.

#### *3.3.2. Cross-section of deformed micropillar*

The bright field image of the deformed pillar is shown in Figure 8(d and e). The slip lines, which were observed in Figure 3(b), are clearly visible on the TEM foil

section. Viewing down the [100] direction, the slip lines make an angle of ~55˚, with the loading direction – this clearly suggests slip on the {111} plane in the micropillar. It is believed that upon compression, slip lines initiate from the side surface of the micropillars and gradually propagate to intersect the top (if the initiation site is close to the top of the pillar). The slip bands in the pillars were observed mostly near the top. The stress (or load, in a load-displacement curve) drop observed consistently in the load-displacement curve is believed to be associated with the initiation of the first slip band. The FIB damaged scale on the pillar wall can possibly act as nucleation site for the bands. However, interestingly, the propagation of the bands was arrested by the shear-zone boundary formed at the top of the micropillar. This horizontal shear zone forms a hardened layer that is 600 nm thick, shown in Supplementary Figure S4 having a distinct misorientation with the rest of the micropillar, as captured in the dark field mode. Interestingly, this hardened surface layer arrests the propagation of the slip bands. This is clearly shown in Figure 8(d). Besides getting interrupted, the slip bands in the present orientation of the micropillar does not form a glide step, which implies that only a part of the induced deformation is localised at the band and there must be other ways the strain is dissipated within the pillar volume. When the bulging of the pillar occurs during homogeneous deformation, following the load drop in the load-displacement plot, some of the γ′ precipitates are also seen to flatten normal to the loading direction. As observed from Figure 8(e), a significant amount of strain is homogeneously distributed in the micropillar section. This is also consistent with the load-displacement curve whereby a steady work hardening of the micropillar is noticed. A very high density of dislocation is observed in the horizontal and vertical γ-channels (Figure 8(e)). However, a significant fraction of the strain also partitioned to the γ′ precipitates, as evident from the strain contrast within γ′ in Figure 8(d). At room temperature, principally octahedral slip on {111} $<1\bar{1}0>$ systems operate in both the phases [1]. Only at higher temperatures, the intermetallic phase becomes stronger than the metallic matrix due to slip of the a/2<101> partials prevalent on the {010} plane besides {111} and thus forming Kear-Wilsdorf (KW) locks. Hence, although a large amount of strain is accommodated in the γ channels, γ′ also deforms under loading. This is visible from the presence of a high density of dislocation shearing the γ′-phase compared to the parent sample. From the observation of Laue spots where the γ′ reflections were observed not to undergo further streaking or shape change after an initial strain, it can be stated that the a$<1\bar{1}0>$ super-dislocation or the

559 a/2<101> partials, in case an APB have been formed, would have glided smoothly on
560 the {111} slip plane with highest Schmid factor without much dislocation interactions
561 due to multiple slips. The observation of high density of dislocation even in the γ′
562 phase observed in the TEM agrees well with the remnant streaking of the Laue peaks
563 after unloading of the micropillar (Figure 6(d)). When viewed down the $[1\bar{1}0]$ zone
564 axis, two sets of slip plane traces are visible as shown in Figure 8(f) shown by arrows.
565 Measuring the angle between the two slip traces (yellow dotted line as guide to the
566 eye) to be ~70˚ the slip planes could be worked out to be (111) and $(11\bar{1})$ in the γ′
567 phase. This is as predicted by the two probable active slip plane from Schmid factor
568 analysis. The stress levels at this small scale are obviously high enough for the
569 dislocations to shear the γ′-precipitates. In this particular TEM sample, we did not see
570 any clear evidence of individual dislocations or pairs in the precipitate phase – this
571 could be attributed to sectioning effect of the TEM foil from a three-dimensional
572 cylindrical pillar. But, particular evidence of the γ′ shearing has been observed from a
573 different micropillar as will be discussed in the later section.
574
575 ***3.3.3. General slip pattern in CMSX-4 micropillar***
576 The activation of single slip in the micropillar of CMSX-4, in general, is
577 consistently observed across different micropillar compression experiments. Time-
578 resolved tracking of micropillar deformation *in-situ* SEM showed the generation of
579 multiple parallel slip lines in the pillar and each clearly associated with a stress drop.
580 Figure 9 shows compliance-corrected engineering stress-strain curve of a square
581 micropillar of dimensions 1.7 μm (width) × 6.8 μm (height), fabricated from the same
582 CMSX-4 sample. It is to be noted that the micropillar was strained until a maximum
583 strain of 25% that is higher than the micro-Laue experiment. During the experiment,
584 three stress drops occurred. In the elastic loading stage, a steady strain is introduced in
585 the pillar – it has been observed previously that within the elastic regime at room
586 temperature load partitions preferentially in the γ′ phase [44] in single crystal CMSX-
587 4. The first stress drop with a magnitude of ~100 MPa (similar to that seen in the
588 cylindrical pillars) is associated during the early stage of yielding, and two other
589 minor events occur during the stage of homogenous deformation. The recorded video
590 of the *in-situ* compression experiment is presented in the Supplementary Video. The
591 snap-shots from the video obtained during the test following the load drops are also
592 shown in the figure. The first stress drop corresponding to a strain of 6% is

accompanied by the formation of a clear slip line on the pillar. This gradually leads to a slip step. In bulk testing, this stress drop, also called yield drop, corresponds to the penetration of dislocation into the γ′ precipitate. Following further deformation, another slip line is formed adjacent to the first one, which indicates slip on a parallel set of {111} planes. The strain in the pillar is primarily accommodated by slip within this deformation band when the final stress drop at 25% strain occurs during the formation of a third slip step in the pillar. Instead of persistent slip on one given plane, the deformed zone is diffused over multiple parallel slip traces, which eventually gives rise to an offset within the final pillar as observed from the image of the deformed pillar after unloading (Figure 9). Also, by this point, other secondary slip systems besides the primary had already started operating, as suggested by the streaking in Laue peaks up to 5% actual strain.

This 25% strained square micropillar was also further sliced and the deformation microstructure studied in the TEM. Figure 10 shows the bright field images, obtained with $\vec{g} = \bar{1}11$ near the $[01\bar{1}]$ zone axis, from a region near the top of the micropillar where no significant strain localisation through slip band formation has taken place and the individual dislocations can be viewed more clearly. Figure 10(a) shows the entire pillar and indicated area (i) in which the deformation has accumulated and (ii) in which individual dislocations can be observed. As usual, the horizontal and vertical γ channels are packed with dislocations at this strain. Within the γ′ precipitate, single dislocation as well as dislocation pairs are clearly seen. These dislocation pairs are partials with a separation distance of ~16nm and bounding an APB. At room temperature APB shearing is the dominant shearing process. As expected, no stacking fault shearing was observed which is generally seen in deformation of bulk sample at high temperatures requiring diffusion processes [54].

During the early stages of deformation, dislocations are confined in the narrow (horizontal and vertical, with respect to the loading axis) γ channels. Up to the yield point, the stress is a response to the accommodation of increasing strain within the γ channels. Upon continued deformation when the dislocation density in the channels increases, the back-stress rises further. Eventually, once a threshold stress is attained, these dislocations are able to overcome the pinning stress at the γ/γ′ interface and penetrate into γ′ precipitates. This happens at the yield point (before the yield drop) where APB shearing takes over as the primary shearing method of the precipitates as dislocations enter in pairs (partials) [1]. Since the stress would be higher to propagate

dislocations for APB shearing, the stress does not drop but instead work hardening is observed until failure of the micropillars (stress *vs* strain curve of Figure 9).

### 3.4. Finite element modeling of the strain within the micropillar

Crystal plasticity modeling of the compression of a micropillar with the exact orientation of [9.95, 0.96, 0.23] oriented with the compression axis confirmed the $(11\bar{1})[101]$ and $(111)[\bar{1}01]$ slip systems with the highest resolved shear stress as also calculated in Table 2. Figure 11 (a and b) shows the strain maps of the $(11\bar{1})[101]$ and $(111)[\bar{1}01]$ slip systems at the point of maximum straining. The discontinuities seen in the strain maps are caused by the pillar being a two-phase material. The small discontinuities seen in the strain maps are the channels that are in between the precipitates. Out of these two slip systems, $(11\bar{1})[101]$ with the higher Schmid factor shows a higher strain intensity. Considering slip on these systems, a homogeneous deformation within the micropillar was observed in modelling the strain distribution with punch displacement. Snapshots of the strain distribution on the two slip systems with increasing punch displacement of 25, 50, 75 and 100% are shown in Supplementary Figure S7. As can be seen clearly, for both the slip systems, a constant accumulation of strain occurs within the pillar that results in bulging of the pillar on the sides – this is in good agreement with the bulging of the micropillar observed in Figure 3(b). The angular profile of the strain with respect to the compression axis gives an indication of the slip trace in the case of a step formation with further straining, as observed in Figure 3(b) and Figure 9. A strain maximum occurs in the centre of the micropillar in both the cases with a conical dead-zone both at the top and bottom of the pillar. However, practically owing to constraints on the top and bottom of the micropillar by the punch and the substrate respectively, some deformation is observed in these areas. While strains arising from frictional forces between the pillar surface and the punch is dominant on the top, a significant reaction force is provided by the surrounding base material to any lateral movement of the micropillar at the bottom – in fact it has been observed that slip bands are formed around the base of the pillar (where the cross-section is larger owing to the presence of a taper in the FIB milled pillar) when substantial deformation occurs [64]. Also depending on the reaction from the substrate to the base of the pillar or the friction

between the punch and pillar top, the position of the maxima is likely to shift from the centre of the pillar.

During *in-situ* deformation, the time-resolved data shown in Figure 6 was acquired from a point ~3.5/4 μm from the top of the micropillar, where the micro-probe was focussed. The position of the strain maxima in the modelled strain map shown in Figure 11 confirmed that the time-resolved data depicted the temporal evolution of deformation from a region in the vicinity of maximum stress in the pillar. A continuous increase in the shear intensity is noted at this location, where the probe was incident in the micropillar indicating a steady homogeneous deformation by glide of dislocations on the two slip planes.

## 4. Conclusion

In summary, we have tested [100]–orientated single crystal Ni-based superalloys CMSX-4 using micropillar compression at room temperature in combination with a variety of *in-situ* and post-deformation characterisation techniques. Using *in-situ* scanning electron microscope and white beam micro-Laue diffraction, followed by post-deformation transmission electron microscopy, a detailed description of the deformation structure within the micropillar volume could be obtained – the observations from these complementary experiments were found to be in good agreement with finite element crystal plasticity modeling. The following conclusions could be drawn from the study:

i. From the analysis of the angular spread in Laue reflections, a two-fold increase in dislocation density – from $2.7\times10^{12}$ to $2.1\times10^{14}$ $m^{-2}$ was obtained readily at a 5% engineering strain under the given loading conditions.

ii. Multiple slip accommodate deformation activates at rather early deformation stages (after 5% engineering strain) but subsequently only the primary slip systems operate (at least until 20% strain).

iii. Slip was primarily accommodated by $(11\bar{1})[101]$ and $(111)[\bar{1}01]$ slip systems having the highest Schmid factor. Easy glide on these slip systems resulted in little accumulation of unpaired GNDs within the micropillar –this was manifested as minimal streaking of the Laue reflections during major part of the loading cycle.

iv. During deformation, independent rotation of the constituent phases was observed and the extent of lattice rotation under uniaxial straining was found to be higher in the

γ-phase as compared to the γ′-phase, given the negative lattice misfit in CMSX-4. A larger lattice rotation in the γ-phase occurred near the base of the pillar.

v. Deformation was mediated through the glide of a/2<110> dislocations on {111} planes in the γ-phase, while owing to high level of stresses in the micropillar even at room temperature, the γ′ are sheared by a/2<110> partials bounding an anti-phase boundary that is free to glide on the {111} plane.

vi. Crystal plasticity finite element modeling of the micropillar compression process showed a uniform strain accumulation in centre of the micropillar for the two slip systems with high Schmid factor. The simulated profile of the strain distribution in the pillar also coincides with the angle of the formation of a glide step observed in the experiments.

*Acknowledgement*

The Engineering and Physical Sciences Research Council (EP/K028707/1 and EP/K034332/1) provided the financial support for the work. The use of Advanced Photon Source (APS) was supported by the U. S. Department of Energy, Office of Science and Office of Basic Energy Sciences, under Contract No. DE-AC02-06CH11357. The authors would also like to thank Dr. Wenjun Liu and Dr. Jon Tischler of beamline 34-ID-E at APS for their generous assistance with the experiments and useful discussions. TBB and SA would like to thank AVIC-BIAM for funding of SA's studentship. TBB would like to thank the Royal Academy of Engineering for funding of his research fellowship.

**Declaration of interest** - None

**Reference**

[1] R.C. Reed, The Superalloys: Fundamentals and Applications, Cambridge University Press, 2006.

[2] C.M.F. Rae, R.C. Reed, Primary creep in single crystal superalloys: Origins, mechanisms and effects, Acta Mater. 55 (2007) 1067–1081. doi:10.1016/j.actamat.2006.09.026.

[3] T. Link, A. Epishin, N. Nawrath, C. Michel, M. Nazmy, Dislocation structures in the gamma prime-phase of CMSX-4 and TMS75after degradation under service conditions, Adv. Mater. Res. 278 (2011) 25–30. doi:10.4028/www.scientific.net/AMR.278.25.

[4] J. Coakley, R.C. Reed, J.L.W. Warwick, K.M. Rahman, D. Dye, Lattice strain evolution during creep in single-crystal superalloys, Acta Mater. 60 (2012)

729 2729–2738. doi:10.1016/j.actamat.2012.01.039.
730 [5] D. Caillard, A. Couret, Chapter 50 Dislocation Cores and Yield Stress
731 Anomalies, in: F.R.N. Nabarro, M.S.B.T.-D. in S. Duesbery (Eds.), L12
732 Ordered Alloy., Elsevier, 1996: pp. 69–134. doi:https://doi.org/10.1016/S1572-
733 4859(96)80005-2.
734 [6] P. Veyssière, G. Saada, Chapter 53 Microscopy and plasticity of the L12
735 γphase, in: F.R.N. Nabarro, M.S.B.T.-D. in S. Duesbery (Eds.), L12 Ordered
736 Alloy., Elsevier, 1996: pp. 253–441. doi:https://doi.org/10.1016/S1572-
737 4859(96)80008-8.
738 [7] T.A. Merz, H. Noad, R. Xu, H. Inoue, W. Liu, Y. Hikita, A. Vailionis, K.A.
739 Moler, H.Y. Hwang, Depth resolved domain mapping in tetragonal SrTiO3 by
740 micro-Laue diffraction, Appl. Phys. Lett. 108 (2016).
741 doi:http://dx.doi.org/10.1063/1.4948351.
742 [8] C. Marichal, H. Van Swygenhoven, S. Van Petegem, C. Borca, {110} Slip with
743 {112} slip traces in bcc Tungsten, Sci. Rep. 3 (2013). doi:10.1038/srep02547.
744 [9] R. Maaß, S. Van Petegem, H. Van Swygenhoven, P.M. Derlet, C.A. Volkert,
745 D. Grolimund, Time-Resolved Laue Diffraction of Deforming Micropillars,
746 Phys. Rev. Lett. 99 (2007) 145505.
747 http://link.aps.org/doi/10.1103/PhysRevLett.99.145505.
748 [10] C. Marichal, K. Srivastava, D. Weygand, S. Van Petegem, D. Grolimund, P.
749 Gumbsch, H. Van Swygenhoven, Origin of anomalous slip in tungsten, Phys.
750 Rev. Lett. 113 (2014). doi:10.1103/PhysRevLett.113.025501.
751 [11] R. Maaß, S. Van Petegem, C.N. Borca, H. Van Swygenhoven, In situ Laue
752 diffraction of metallic micropillars, Mater. Sci. Eng. A. 524 (2009) 40–45.
753 doi:http://dx.doi.org/10.1016/j.msea.2009.05.062.
754 [12] C. Leclere, T.W. Cornelius, Z. Ren, A. Davydok, J.-S. Micha, O. Robach, G.
755 Richter, L. Belliard, O. Thomas, In-situ bending of an Au nanowire monitored
756 by micro Laue diffraction, J. Appl. Crystallogr. 48 (2015) 291–296.
757 doi:10.1107/S1600576715001107.
758 [13] J. Gamcová, G. Mohanty, Š. Michalik, J. Wehrs, J. Bednarčík, C. Krywka, J.M.
759 Breguet, J. Michler, H. Franz, Mapping strain fields induced in Zr-based bulk
760 metallic glasses during in-situ nanoindentation by X-ray nanodiffraction, Appl.
761 Phys. Lett. 108 (2016). doi:http://dx.doi.org/10.1063/1.4939981.
762 [14] R.I. Barabash, G.E. Ice, F.J. Walker, Quantitative microdiffraction from
763 deformed crystals with unpaired dislocations and dislocation walls, J. Appl.
764 Phys. 93 (2003) 1457–1464. doi:10.1063/1.1534378.
765 [15] F. Hofmann, X. Song, I. Dolbnya, B. Abbey, A.M. Korsunsky, Probing intra-
766 granular deformation by micro-beam Laue diffraction, Procedia Eng. 1 (2009)
767 193–196. doi:http://dx.doi.org/10.1016/j.proeng.2009.06.045.
768 [16] J.M. Wheeler, C. Niederberger, C. Tessarek, S. Christiansen, J. Michler,
769 Extraction of plasticity parameters of GaN with high temperature, in situ
770 micro-compression, Int. J. Plast. 40 (2013) 140–151.
771 doi:https://doi.org/10.1016/j.ijplas.2012.08.001.
772 [17] J.J. Roa, J.M. Wheeler, T. Trifonov, G. Fargas, A. Mateo, J. Michler, E.
773 Jiménez-Piqué, Deformation of polycrystalline TRIP stainless steel
774 micropillars, Mater. Sci. Eng. A. 647 (2015) 51–57.
775 doi:http://dx.doi.org/10.1016/j.msea.2015.08.082.
776 [18] H. Ghassemi-Armaki, R. Maaß, S.P. Bhat, S. Sriram, J.R. Greer, K.S. Kumar,
777 Deformation response of ferrite and martensite in a dual-phase steel, Acta
778 Mater. 62 (2014) 197–211.

779 doi:http://dx.doi.org/10.1016/j.actamat.2013.10.001.
780 [19] J. Wang, N. Stanford, Investigation of precipitate hardening of slip and
781 twinning in Mg5%Zn by micropillar compression, Acta Mater. 100 (2015) 53–
782 63. doi:10.1016/j.actamat.2015.08.012.
783 [20] H.E. Weekes, V.A. Vorontsov, I.P. Dolbnya, J.D. Plummer, F. Giuliani, T.B.
784 Britton, D. Dye, In situ micropillar deformation of hydrides in Zircaloy-4, Acta
785 Mater. 92 (2015) 81–96. doi:http://dx.doi.org/10.1016/j.actamat.2015.03.037.
786 [21] R. Gu, A.H.W. Ngan, Size effect on the deformation behavior of duralumin
787 micropillars, Scr. Mater. 68 (2013) 861–864.
788 doi:10.1016/j.scriptamat.2013.02.012.
789 [22] X.B. Feng, J.Y. Zhang, Y.Q. Wang, Z.Q. Hou, K. Wu, G. Liu, J. Sun, Size
790 effects on the mechanical properties of nanocrystalline NbMoTaW refractory
791 high entropy alloy thin films, Int. J. Plast. 95 (2017) 264–277.
792 doi:https://doi.org/10.1016/j.ijplas.2017.04.013.
793 [23] T.-S. Jun, Z. Zhang, G. Sernicola, F.P.E. Dunne, T.B. Britton, Local strain rate
794 sensitivity of single α phase within a dual-phase Ti alloy, Acta Mater. 107
795 (2016) 298–309. doi:10.1016/j.actamat.2016.01.057.
796 [24] A.J. Knowles, T.-S. Jun, A. Bhowmik, N.G. Jones, T. Ben Britton, F. Giuliani,
797 H.J. Stone, D. Dye, A new beta titanium alloy system reinforced with
798 superlattice intermetallic precipitates, Scr. Mater. 140 (2017) 71–75.
799 doi:https://doi.org/10.1016/j.scriptamat.2017.06.038.
800 [25] F. Hofmann, S. Keegan, A.M. Korsunsky, Diffraction post-processing of 3D
801 dislocation dynamics simulations for direct comparison with micro-beam Laue
802 experiments, Mater. Lett. 89 (2012) 66–69.
803 doi:https://doi.org/10.1016/j.matlet.2012.08.052.
804 [26] A. Bhowmik, I.P. Dolbnya, T. Ben Britton, N.G. Jones, G. Sernicola, C.
805 Walter, P. Gille, D. Dye, W.J. Clegg, F. Giuliani, Using coupled micropillar
806 compression and micro-Laue diffraction to investigate deformation
807 mechanisms in a complex metallic alloy Al13Co4, Appl. Phys. Lett. 108
808 (2016). doi:http://dx.doi.org/10.1063/1.4944486.
809 [27] A. Bhowmik, J. Lee, T. Ben Britton, W. Liu, T.-S. Jun, G. Sernicola, M.
810 Karimpour, D.S. Balint, F. Giuliani, Deformation behaviour of [001] oriented
811 MgO using combined in-situ nano-indentation and micro-Laue diffraction,
812 Acta Mater. 145 (2018) 516–531.
813 doi:https://doi.org/10.1016/j.actamat.2017.12.002.
814 [28] R. Maaß, M.D. Uchic, In-situ characterization of the dislocation-structure
815 evolution in Ni micro-pillars, Acta Mater. 60 (2012) 1027–1037.
816 doi:http://dx.doi.org/10.1016/j.actamat.2011.11.007.
817 [29] J. Zimmermann, S. Van Petegem, H. Bei, D. Grolimund, E.P. George, H. Van
818 Swygenhoven, Effects of focused ion beam milling and pre-straining on the
819 microstructure of directionally solidified molybdenum pillars: A Laue
820 diffraction analysis, Scr. Mater. 62 (2010) 746–749.
821 doi:http://dx.doi.org/10.1016/j.scriptamat.2010.02.013.
822 [30] C. Kirchlechner, P.J. Imrich, W. Grosinger, M.W. Kapp, J. Keckes, J.S. Micha,
823 O. Ulrich, O. Thomas, S. Labat, C. Motz, G. Dehm, Expected and unexpected
824 plastic behavior at the micron scale: An in situ μLaue tensile study, Acta
825 Mater. 60 (2012) 1252–1258.
826 doi:http://dx.doi.org/10.1016/j.actamat.2011.10.058.
827 [31] G.E. Ice, J.W.L. Pang, Tutorial on x-ray microLaue diffraction, Mater. Charact.
828 60 (2009) 1191–1201. doi:http://dx.doi.org/10.1016/j.matchar.2009.07.006.

[32] R. Barabash, G.E. Ice, B.C. Larson, G.M. Pharr, K.-S. Chung, W. Yang, White microbeam diffraction from distorted crystals, Appl. Phys. Lett. 79 (2001) 749–751. doi:doi:http://dx.doi.org/10.1063/1.1389321.
[33] P.A. Shade, M.D. Uchic, D.M. Dimiduk, G.B. Viswanathan, R. Wheeler, H.L. Fraser, Size-affected single-slip behavior of René N5 microcrystals, Mater. Sci. Eng. A. 535 (2012) 53–61. doi:https://doi.org/10.1016/j.msea.2011.12.041.
[34] K. Arora, K. Kishida, K. Tanaka, H. Inui, Effects of lattice misfit on plastic deformation behavior of single-crystalline micropillars of Ni-based superalloys, Acta Mater. 138 (2017) 119–130. doi:https://doi.org/10.1016/j.actamat.2017.07.044.
[35] M.D. Uchic, D.M. Dimiduk, A methodology to investigate size scale effects in crystalline plasticity using uniaxial compression testing, Mater. Sci. Eng. A. 400–401 (2005) 268–278. doi:https://doi.org/10.1016/j.msea.2005.03.082.
[36] R.J. Asaro, Crystal Plasticity, J. Appl. Mech. 50 (1983) 921–934. http://dx.doi.org/10.1115/1.3167205.
[37] D. Peirce, R.J. Asaro, A. Needleman, Material rate dependence and localized deformation in crystalline solids, Acta Metall. 31 (1983) 1951–1976. doi:http://dx.doi.org/10.1016/0001-6160(83)90014-7.
[38] S. Keshavarz, S. Ghosh, A.C.E. Reid, S.A. Langer, A non-Schmid crystal plasticity finite element approach to multi-scale modeling of nickel-based superalloys, Acta Mater. 114 (2016) 106–115. doi:https://doi.org/10.1016/j.actamat.2016.05.016.
[39] S. Keshavarz, S. Ghosh, Multi-scale crystal plasticity finite element model approach to modeling nickel-based superalloys, Acta Mater. 61 (2013) 6549–6561. doi:https://doi.org/10.1016/j.actamat.2013.07.038.
[40] Y. Huang, A User-material Subroutine Incroporating Single Crystal Plasticity in the ABAQUS Finite Element Program., (1991).
[41] B. Eidel, Crystal plasticity finite-element analysis versus experimental results of pyramidal indentation into (0 0 1) fcc single crystal, Acta Mater. 59 (2011) 1761–1771. doi:http://dx.doi.org/10.1016/j.actamat.2010.11.042.
[42] Z. Zhang, T.-S. Jun, T.B. Britton, F.P.E. Dunne, Intrinsic anisotropy of strain rate sensitivity in single crystal alpha titanium, Acta Mater. 118 (2016) 317–330. doi:http://dx.doi.org/10.1016/j.actamat.2016.07.044.
[43] D. Siebörger, H. Knake, U. Glatzel, Temperature dependence of the elastic moduli of the nickel-base superalloy CMSX-4 and its isolated phases, Mater. Sci. Eng. A. 298 (2001) 26–33. doi:http://dx.doi.org/10.1016/S0921-5093(00)01318-6.
[44] D. Dye, J. Coakley, V.A. Vorontsov, H.J. Stone, R.B. Rogge, Elastic moduli and load partitioning in a single-crystal nickel superalloy, Scr. Mater. 61 (2009) 109–112. doi:http://dx.doi.org/10.1016/j.scriptamat.2009.03.008.
[45] E. Wu, G. Sun, B. Chen, T. Pirling, D.J. Hughes, S. Wang, J. Zhang, A neutron diffraction study of lattice distortion, mismatch and misorientation in a single-crystal superalloy after different heat treatments, Acta Mater. 61 (2013) 2308–2319. doi:http://dx.doi.org/10.1016/j.actamat.2013.01.001.
[46] C. Lang, W. Schneider, H. Mughrab, X-ray investigations on creep-deformed single crystals of the nickel—base superalloy CMSX-4, Acta Metall. Mater. 43 (1995) 1751–1764. doi:http://dx.doi.org/10.1016/0956-7151(94)00407-9.
[47] F. Pyczak, B. Devrient, H. Mughrabi, The effects of different alloying elements on the thermal expansion coefficients, lattice constants and misfit of nickel-based superalloys investigated by X-ray diffraction, in: Proc. Int. Symp.

Superalloys, 2004: pp. 827–836. https://www.scopus.com/inward/record.uri?eid=2-s2.0-22744431548&partnerID=40&md5=d884046838b2b428ed9b744dc50d35e3.
[48] H. Bei, S. Shim, M.K. Miller, G.M. Pharr, E.P. George, Effects of focused ion beam milling on the nanomechanical behavior of a molybdenum-alloy single crystal, Appl. Phys. Lett. 91 (2007). doi:http://dx.doi.org/10.1063/1.2784948.
[49] W.J. MoberlyChan, D.P. Adams, M.J. Aziz, G. Hobler, T. Schenkel, Fundamentals of Focused Ion Beam Nanostructural Processing: Below, At, and Above the Surface, MRS Bull. 32 (2007) 424–432. doi:doi:10.1557/mrs2007.66.
[50] G.E. Ice, R.I. Barabash, Chapter 79 White Beam Microdiffraction and Dislocations Gradients, in: F.R.N.N. and J.P.H.B.T.-D. in Solids (Ed.), Dislocations in Solid, Elsevier, 2007: pp. 499–601. doi:http://dx.doi.org/10.1016/S1572-4859(07)80011-8.
[51] C. Kirchlechner, J. Keckes, C. Motz, W. Grosinger, M.W. Kapp, J.S. Micha, O. Ulrich, G. Dehm, Impact of instrumental constraints and imperfections on the dislocation structure in micron-sized Cu compression pillars, Acta Mater. 59 (2011) 5618–5626. doi:10.1016/j.actamat.2011.05.037.
[52] E.F. Westbrooke, L.E. Forero, F. Ebrahimi, Slip analysis in a Ni-base superalloy, Acta Mater. 53 (2005) 2137–2147. doi:https://doi.org/10.1016/j.actamat.2005.01.025.
[53] A. Sengupta, S.K. Putatunda, L. Bartosiewicz, J. Hangas, P.J. Nailos, M. Peputapeck, F.E. Alberts, Tensile behavior of a new single-crystal nickel-based superalloy (CMSX-4) at room and elevated temperatures, J. Mater. Eng. Perform. 3 (1994) 73–81. doi:10.1007/BF02654502.
[54] M. Feller-Kniepmeier, T. Link, I. Poschmann, G. Scheunemann-Frerker, C. Schulze, Temperature dependence of deformation mechanisms in a single crystal nickel-base alloy with high volume fraction of γ′ phase, Acta Mater. 44 (1996) 2397–2407. doi:https://doi.org/10.1016/1359-6454(95)00354-1.
[55] N.S. Husseini, D.P. Kumah, J.Z. Yi, C.J. Torbet, D.A. Arms, E.M. Dufresne, T.M. Pollock, J. Wayne Jones, R. Clarke, Mapping single-crystal dendritic microstructure and defects in nickel-base superalloys with synchrotron radiation, Acta Mater. 56 (2008) 4715–4723. doi:https://doi.org/10.1016/j.actamat.2008.05.041.
[56] L. Liu, N.S. Husseini, C.J. Torbet, W.-K. Lee, R. Clarke, J.W. Jones, T.M. Pollock, In situ synchrotron X-ray imaging of high-cycle fatigue crack propagation in single-crystal nickel-base alloys, Acta Mater. 59 (2011) 5103–5115. doi:https://doi.org/10.1016/j.actamat.2011.04.042.
[57] H. Biermann, B. von Grossmann, T. Ungár, S. Mechsner, A. Souvorov, M. Drakopoulos, A. Snigirev, H. Mughrabi, Determination of local strains in a monocrystalline turbine blade by microbeam X-ray diffraction with synchrotron radiation, Acta Mater. 48 (2000) 2221–2230. doi:https://doi.org/10.1016/S1359-6454(00)00038-0.
[58] J.-B. le Graverend, A. Jacques, J. Cormier, O. Ferry, T. Schenk, J. Mendez, Creep of a nickel-based single-crystal superalloy during very high-temperature jumps followed by synchrotron X-ray diffraction, Acta Mater. 84 (2015) 65–79. doi:https://doi.org/10.1016/j.actamat.2014.10.036.
[59] A. Royer, P. Bastie, M. Véron, Temperature dependence of superstructure and fundamental reflections: study of a creep deformed single crystal nickel base superalloy AM1, Mater. Sci. Eng. A. 234–236 (1997) 1110–1113.

doi:https://doi.org/10.1016/S0921-5093(97)00341-9.
[60] C. Schwalbe, A. Jacques, E. Galindo-Nava, C.N. Jones, C.M.F. Rae, J. Cormier, In situ measurement of the precipitate volume fraction and interfacial lattice misfit during non-isothermal creep in the superalloy CMSX-4, Mater. Sci. Eng. A. 740–741 (2019) 182–186. doi:https://doi.org/10.1016/j.msea.2018.10.033.
[61] A. Davydok, B.N. Jaya, O. Robach, O. Ulrich, J.-S. Micha, C. Kirchlechner, Analysis of the full stress tensor in a micropillar: Ability of and difficulties arising during synchrotron based μLaue diffraction, Mater. Des. 108 (2016) 68–75. doi:https://doi.org/10.1016/j.matdes.2016.06.098.
[62] A. Luft, Microstructural processes of plastic instabilities in strengthened metals, Prog. Mater. Sci. 35 (1991) 97–204. doi:https://doi.org/10.1016/0079-6425(91)90002-B.
[63] P. Zhang, Y. Yuan, B. Li, G. Yang, X. Song, Investigation of tensile deformation mechanisms at room temperature in a new Ni-based single crystal superalloy, Philos. Mag. Lett. 96 (2016) 238–245. doi:10.1080/09500839.2016.1195931.
[64] S. Korte, M. Ritter, C. Jiao, P.A. Midgley, W.J. Clegg, Three-dimensional electron backscattered diffraction analysis of deformation in MgO micropillars, Acta Mater. 59 (2011) 7241–7254. doi:http://dx.doi.org/10.1016/j.actamat.2011.08.022.

952 Table 1. Material parameters used in the CPFE model in this study.

| Parameter | Channel | Precipitates |
|---|---|---|
| $C_{11}$ (GPa) | 252.0 | 252.0 |
| $C_{12}$ (GPa) | 161.0 | 161.0 |
| $C_{44}$ (GPa) | 131.0 | 131.0 |
| Slip system | $\{111\} < \bar{1}10 >$ | $\{111\} < \bar{1}10 >$ |
| $\tau_0$ (MPa) | 775.0 | 1550.0 |
| $\tau_s$ (MPa) | 975.0 | 1850.0 |
| $h_0$ (MPa) | 350.0 | 350.0 |
| $\dot{a}$ | 0.001 | 0.001 |
| $n$ | 20.0 | 20.0 |
| $q$ | 1.4 | 1.4 |

953
954 Table 2: Schmid factor for all the 12 slip systems in A1-$L1_2$ phase in CMSX-4 with
955 the [9.95, 0.96, 0.23] as compression axis

| Slip Systems | Schmid Factors |
|---|---|
| $(111)[\bar{1}01]$ | 0.442 |
| $(111)[0\bar{1}1]$ | 0.033 |
| $(111)[\bar{1}10]$ | 0.409 |
| $(1\bar{1}1)[\bar{1}01]$ | 0.366 |
| $(1\bar{1}1)[011]$ | 0.045 |
| $(1\bar{1}1)[110]$ | 0.411 |
| $(\bar{1}11)[0\bar{1}1]$ | 0.026 |
| $(\bar{1}11)[110]$ | 0.390 |
| $(\bar{1}11)[101]$ | 0.364 |
| $(11\bar{1})[\bar{1}10]$ | 0.392 |
| $(11\bar{1})[101]$ | 0.444 |
| $(11\bar{1})[011]$ | 0.052 |

956

# Appendix

## Method for compliance correction of testing rig

A separate experiment with a pillar diameter of 4.7μm and height of 8μm was performed in a displacement-controlled mode with the Alemnis loading rig inside an FEI Quanta environmental field emission gun-SEM. The pillar was compressed up to a punch displacement of 0.5 μm. The raw load-displacement curve obtained from this pillar, shown in Appendix Figure A1(a), was similar to the 4 μm pillar with a load drop occurring near the yield point – however, this drop was smaller corresponding to stress drop of ~40 MPa. In this case, from the test video (Supplementary video) captured, the stiffness of loading rig was calculated by tracking the movement of the whole sample in the frames. A 0.16 μm depression of the loading stage was noted from the video at the maximum displacement (0.5 μm) of the punch. Then, by offsetting this additional movement of the substrate (with the frames) from the total displacement of the punch, the actual displacement of the micropillar and hence the actual strain in the sample could was obtained. Following this corrective measure, the stress-strain plot was redrawn and compared with the uncorrected data in Figure A1(b) and it is obvious from the figure that the actual pillar response is much stiffer. For a sanity check, the yield stress from the data was compared with the literature data available for CMSX-4 and was found to be in reasonable correspondence.
The same exercise was carried out with the micropillar experiment performed in the beamline. Since the compression experiment could not be visually tracked in this case, an extrapolated value of the substrate depression for 2 μm displacement of the punch was used for correction. The engineering stress-strain curve obtained in for this case is shown in Figure A1(c).

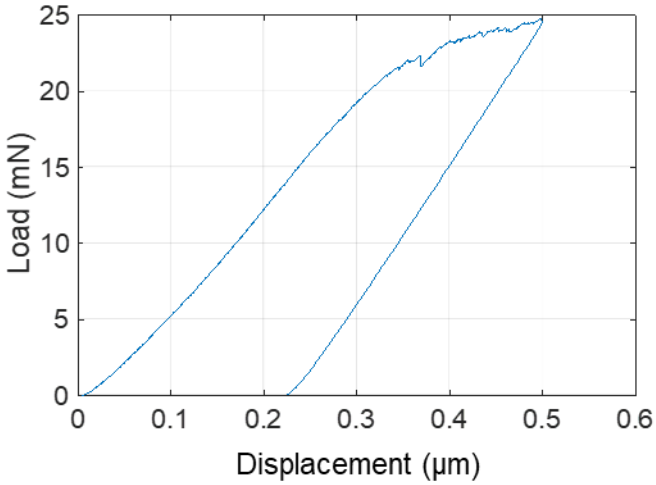


(a)

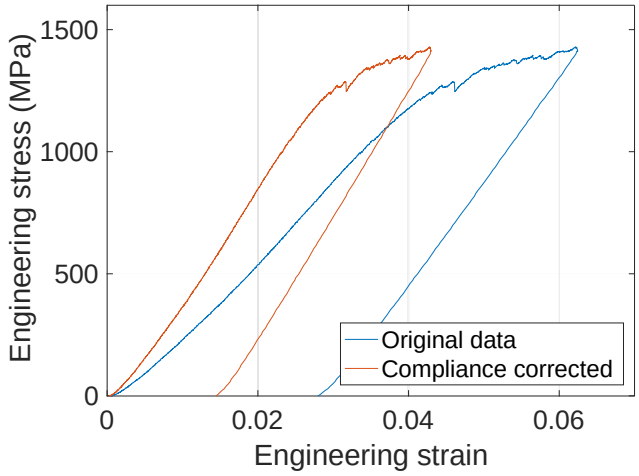


(b)

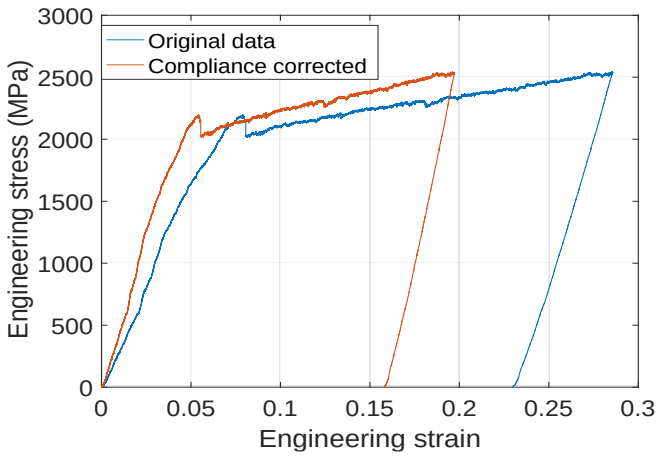


(c)

Appendix Figure A1. (a) The original load-displacement plot obtained from in-situ SEM compression of micropillar. A comparison of the original data and compliance corrected stress-strain curves obtained from compression of the micropillar *in-situ* (b) SEM and (c) beamline micro-Laue experiment.

# Appendix

## Method for compliance correction of testing rig

A separate experiment with a pillar diameter of 4.7µm and height of 8µm was performed in a displacement-controlled mode with the Alemnis loading rig inside an FEI Quanta environmental field emission gun-SEM. The pillar was compressed up to a punch displacement of 0.5 µm. The raw load-displacement curve obtained from this pillar, shown in Appendix Figure A1(a), was similar to the 4µm pillar with a load drop occurring near the yield point – however, the load drop was smaller corresponding to stress drop of ~40 MPa. In this case, from the test video (Supplementary video) captured, the stiffness of loading rig was calculated by tracking the movement of the whole sample in the frames. A 0.16 µm depression of the loading stage was noted from the video at the maximum displacement (0.5 µm) of the punch. Then, by offsetting this additional movement of the substrate (with the frames) from the total displacement of the punch, the actual displacement of the micropillar and hence the actual strain in the sample could was obtained. Following this corrective measure, the stress-strain plot was redrawn and compared with the uncorrected data in Figure A1(b) and it is obvious from the figure that the actual pillar response is much stiffer. For a sanity check, the yield stress from the data was compared with the literature data available for CMSX-4 and was found to be in reasonable correspondence.

The same exercise was carried out with the micropillar experiment performed in the beamline. Since the compression experiment could not be visually tracked in this case, an extrapolated value of the substrate depression for 2 µm displacement of the punch was used for correction. The engineering stress-strain curve obtained in for this case is shown in Figure A1(c).

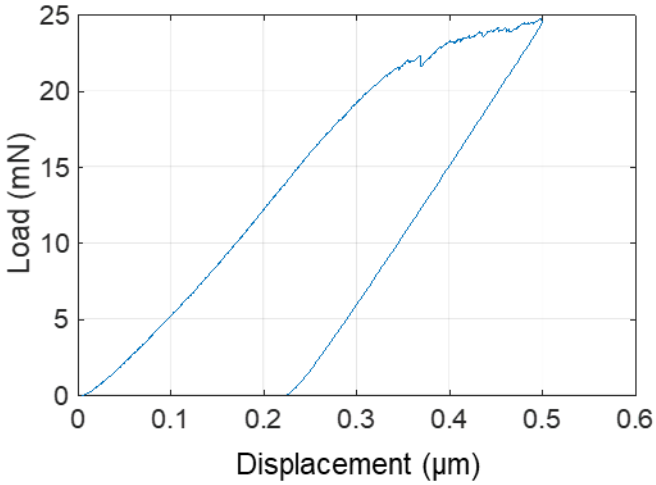


(a)

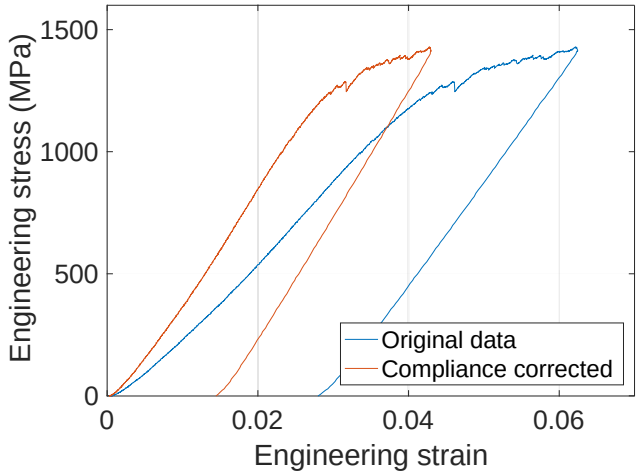


(b)

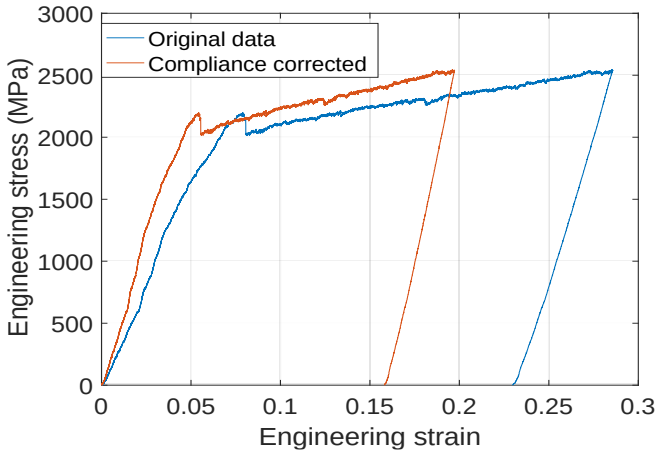


(c)

Appendix Figure A1. (a) The original load-displacement plot obtained from in-situ SEM compression of micropillar. A comparison of the original data and compliance corrected stress-strain curves obtained from compression of the micropillar *in-situ* (b) SEM and (c) beamline micro-Laue experiment.

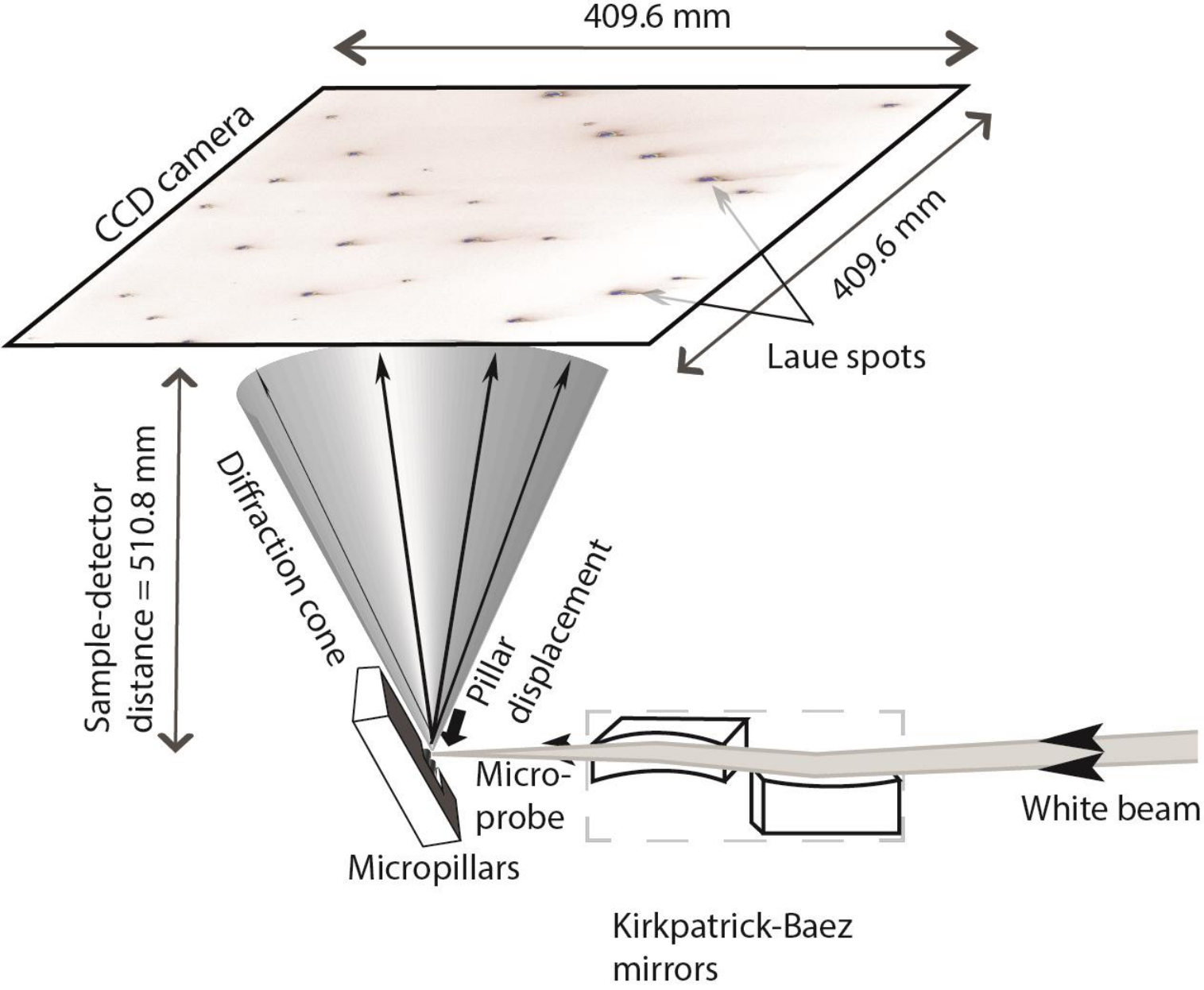


FIGURE 1. Schematic of the experimental set up for the combined micropillar compression and microLaue diffraction. The incident white beam had an energy range of 7-30 keV with the focused probe of size of 0.4 µm × 0.4 µm. The block arrow denotes the compression direction.

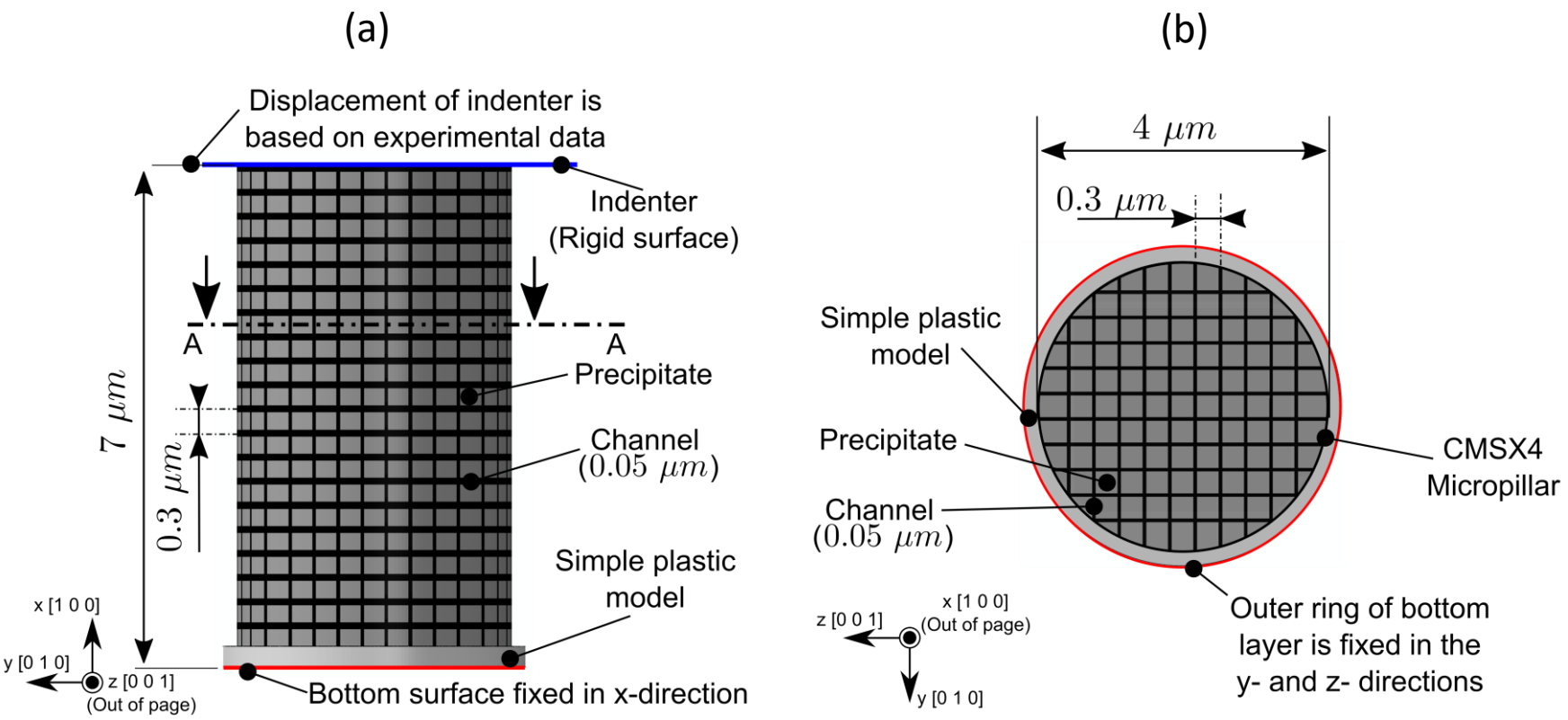


FIGURE 2. Finite element model and the relevant boundary conditions (a) Front view (b) Bottom view.

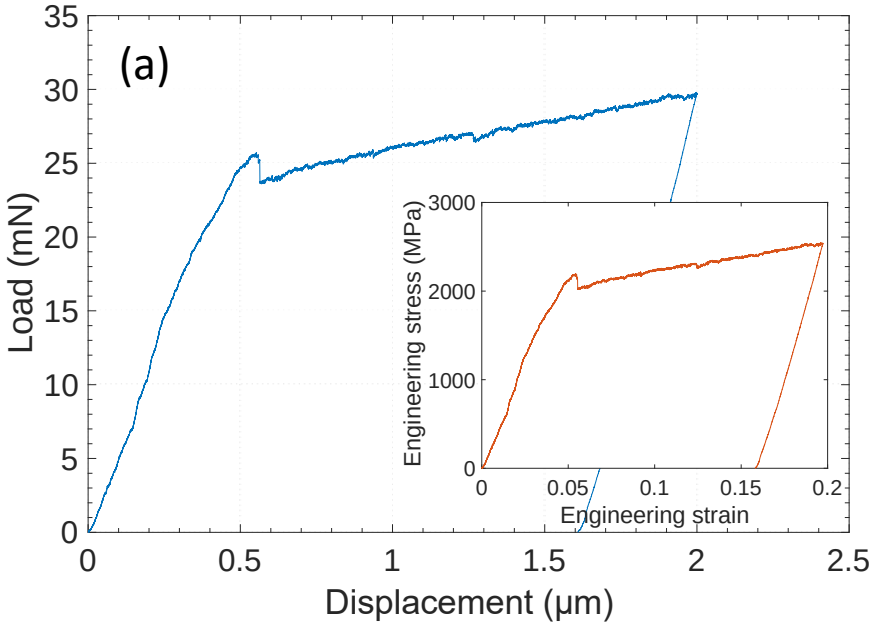


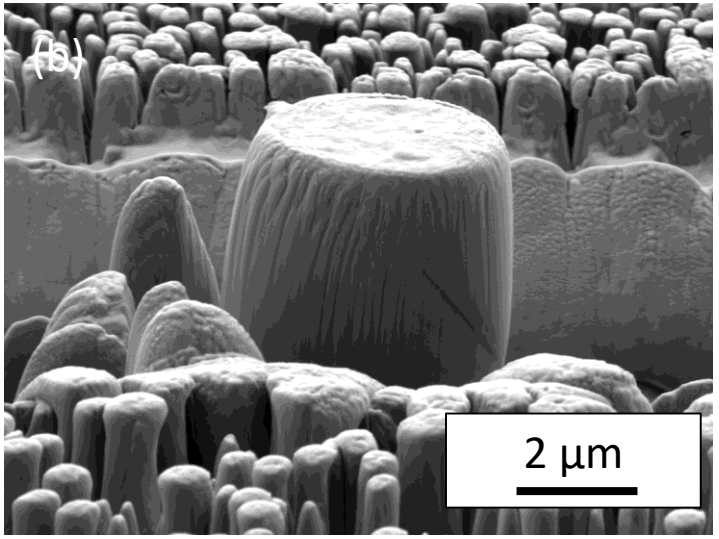


FIGURE 3. (a) Original load-displacement curves for for the CMSX 4 [100] micropillar tested during diffraction experiment with the compliance corrected engineering stress-strain curve in the inset. (b) SEM image of the compressed micropillar showing the occurrence of slip bands on the surface and also notable bulging.

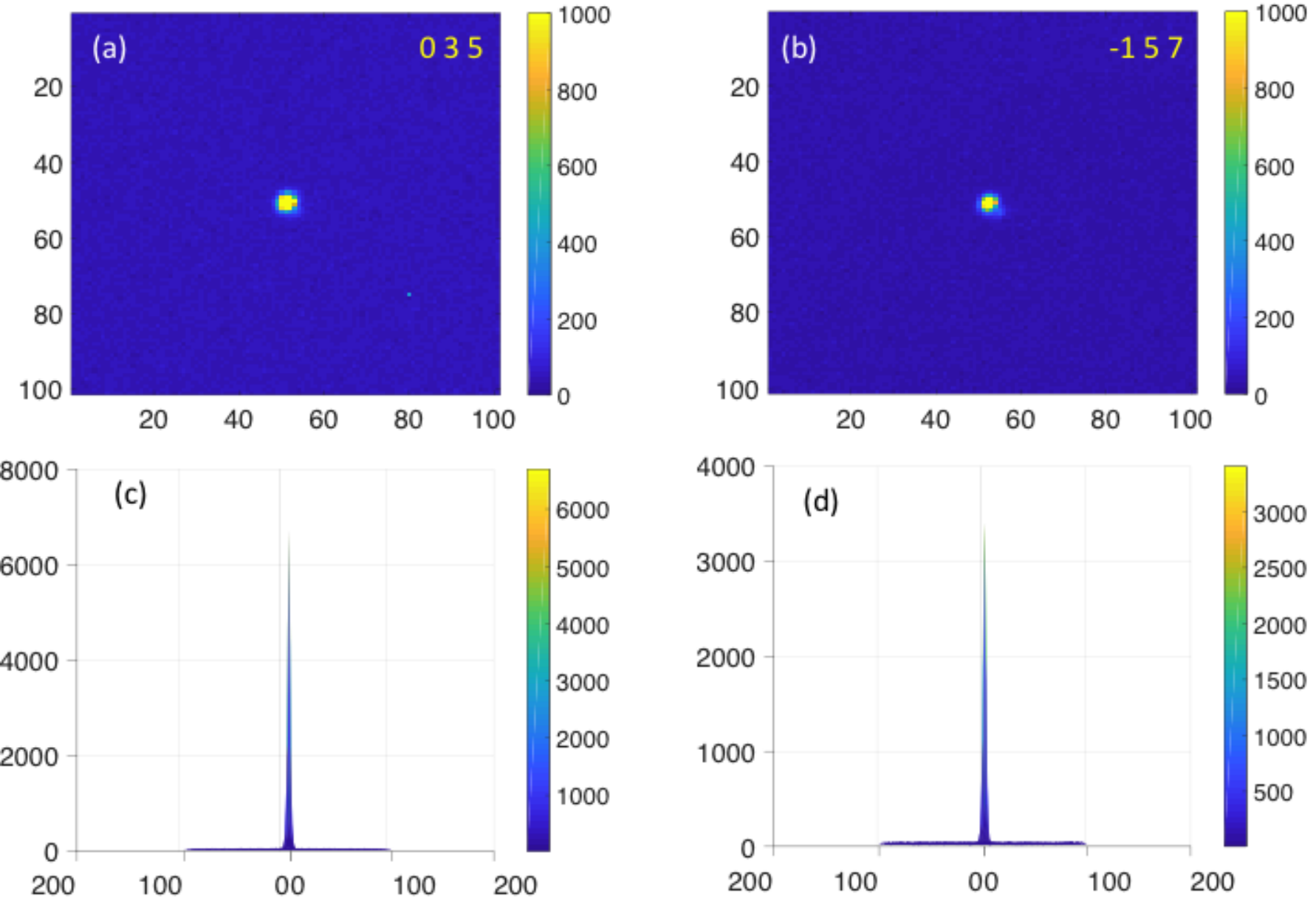


FIGURE 4. (a and b) Laue reflections from two Si peaks peaks showing the symmetrical distribution of intensity. The insets show the peaks in three dimension. (c and d) Sectioned profile of the peaks in a and b respectively.

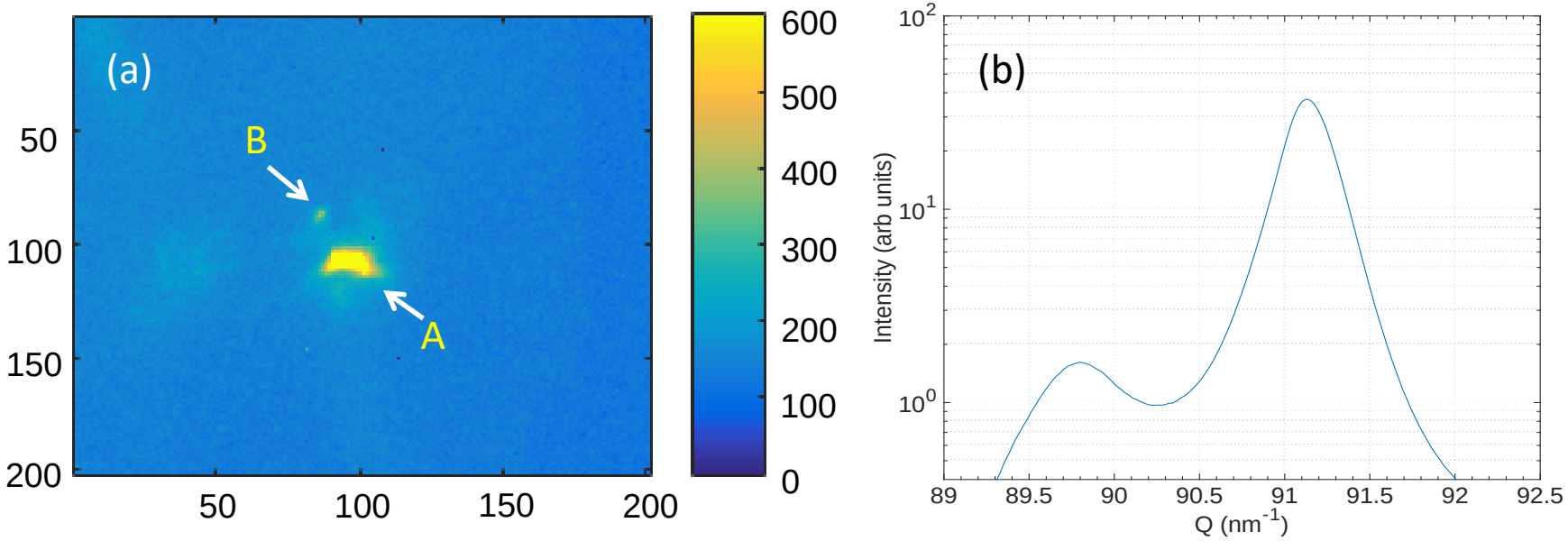


FIGURE 5. (a) -119 peak from from the parent micropillar prior to compression. The reflections A and B belong to the γ' and γ phases respectively. (b) The intensity vs Q (= $4\pi sin\theta/\lambda$) plot obtained from narrow band energy scan of 15.3±0.3 keV with a step size of 0.003 keV corresponding to the -115 peak

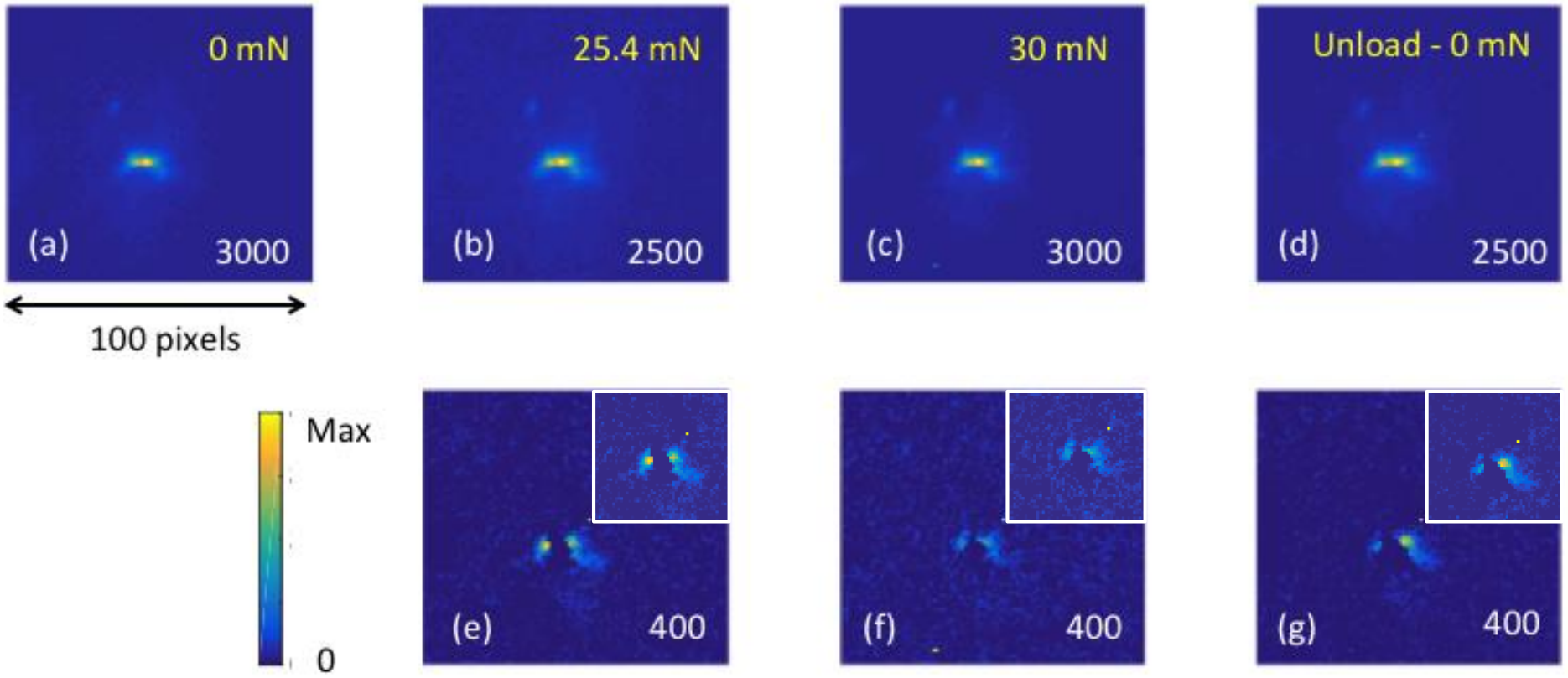


FIGURE 6. (a-d) Time-resolved Laue pattern showing the evolution of the -119 peak during compression of the micropillar upto peak load till unloading. The exposure time for each frame was 4s. (e-g) The residual obtained by subtracting the frames upon loading form the initial frame. The insets in (e-g) show the residuals in 50 x 50 pixel frames for better clarity. Note the numbers on the bottom right corners indicate the maximum value of intensity ('Max' value on the intensity index) for each frame.

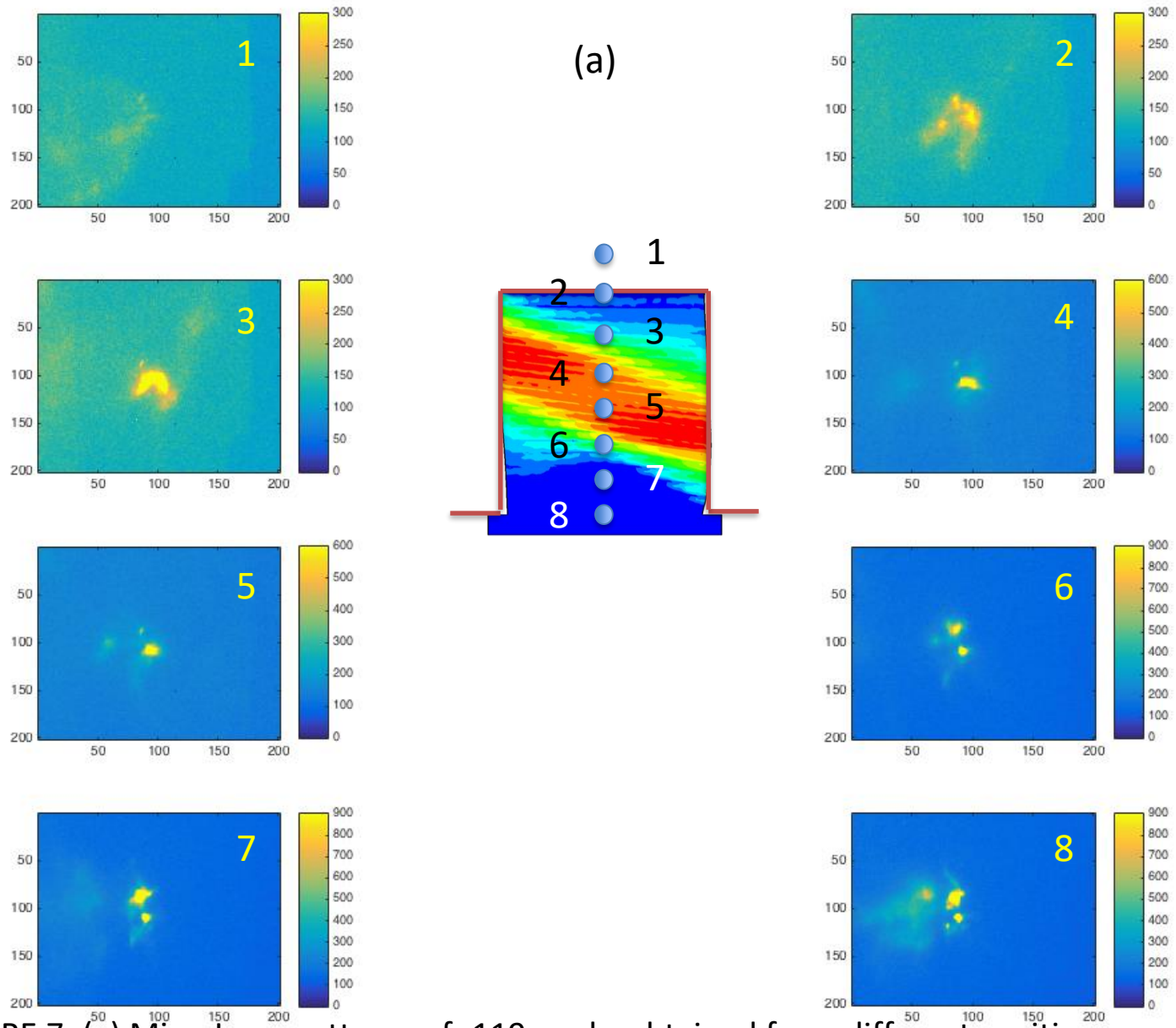


FIGURE 7. (a) MicroLaue patterns of -119 peaks obtained from different positions, marked 1-8, along the vertical axis of the compressed micropillar sample. The patterns, numbered 1 to 8, were taken with a step of 1 µm.

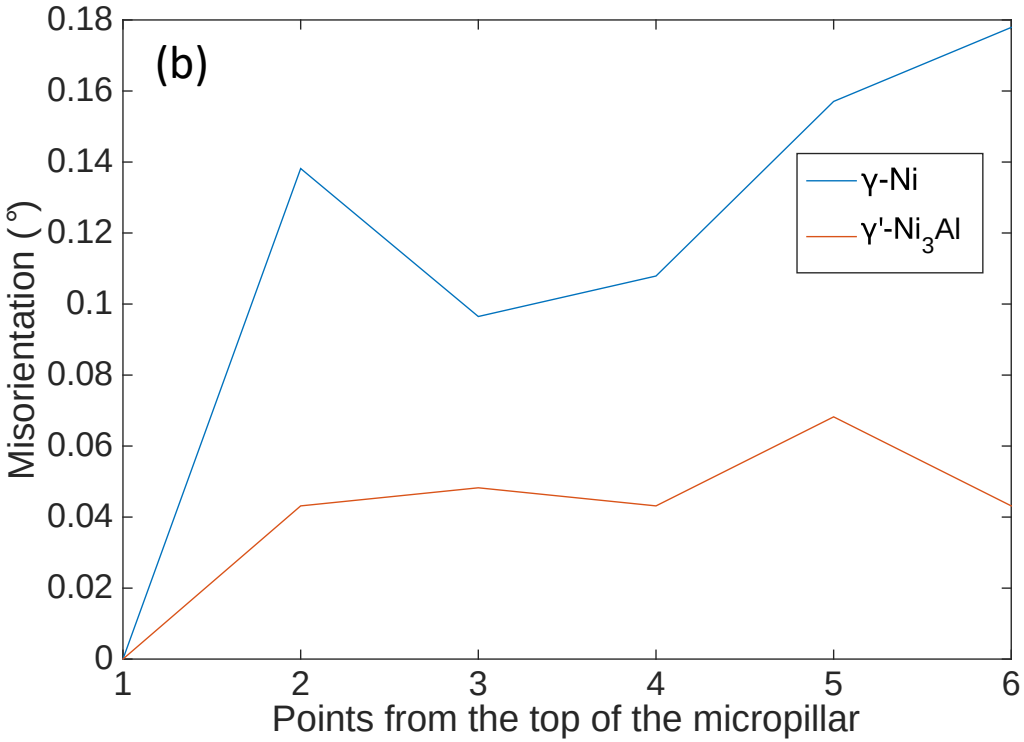


FIGURE 7. (b) Misorientation of the two phases measured along the axis of the pillar.

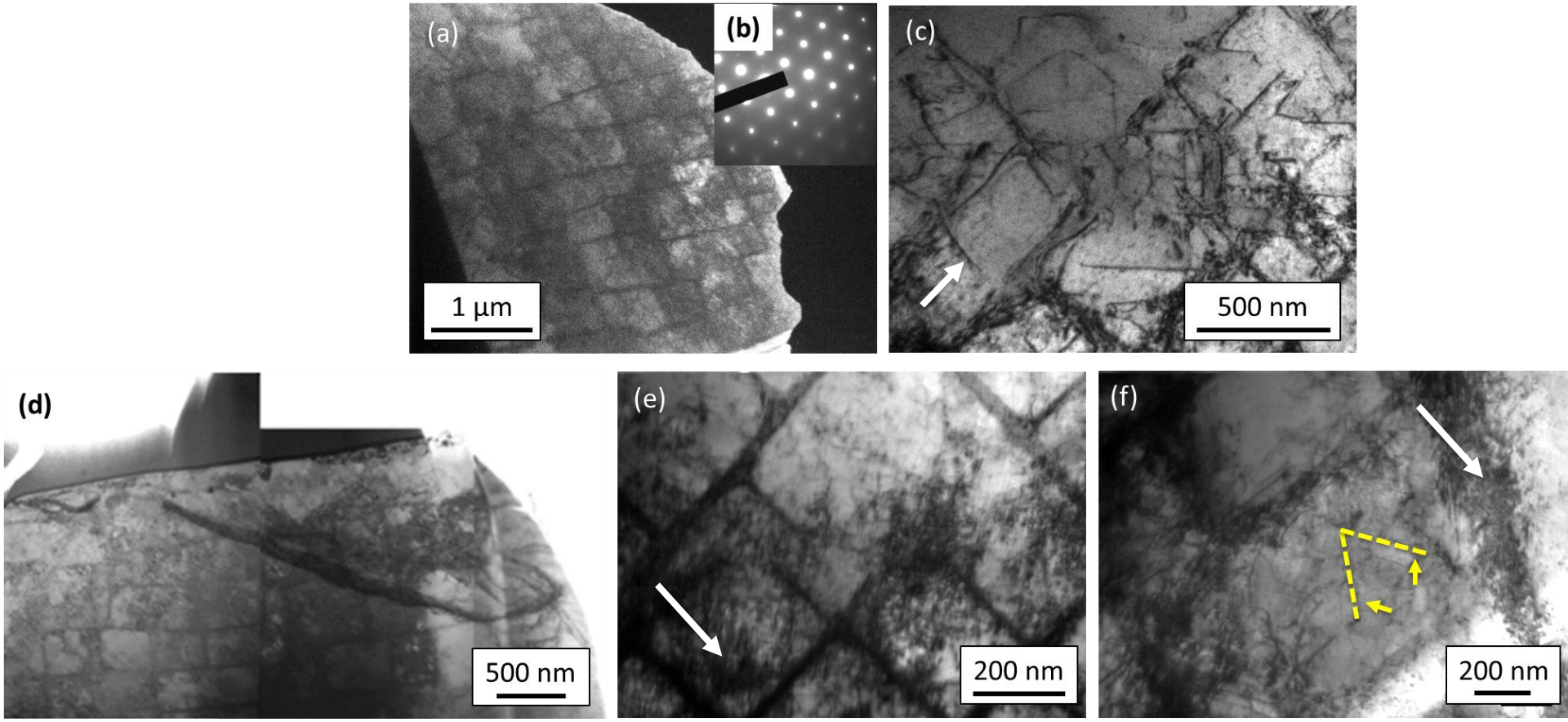


FIGURE 8. (a) TEM dark-field image obtained using -111 reflection of the parent CMSX 4 micropillar viewing down the (b) [110] zone axis. (c) Bright field image of the prior microstructure shown the presence of long threads of dislocations already in the sample. The white arrow is the $\vec{g}$=-111 vector (d) Bright field image of the section from the deformed micropillar. The slip band, seen in the SEM image in Figure 3, is also visible. Note that the slip band do not produce a glide step and also gets terminated at the top friction zone of the micropillar. (e) A high density of dislocations are observed in both the γ channels, showing a dark contrast, and also in the γ' phase. (f) Within the γ' phase, traces of intersecting {111} planes viewing down close to <1-10> zone. The direction of $\vec{g}$=-002 vector is shown.

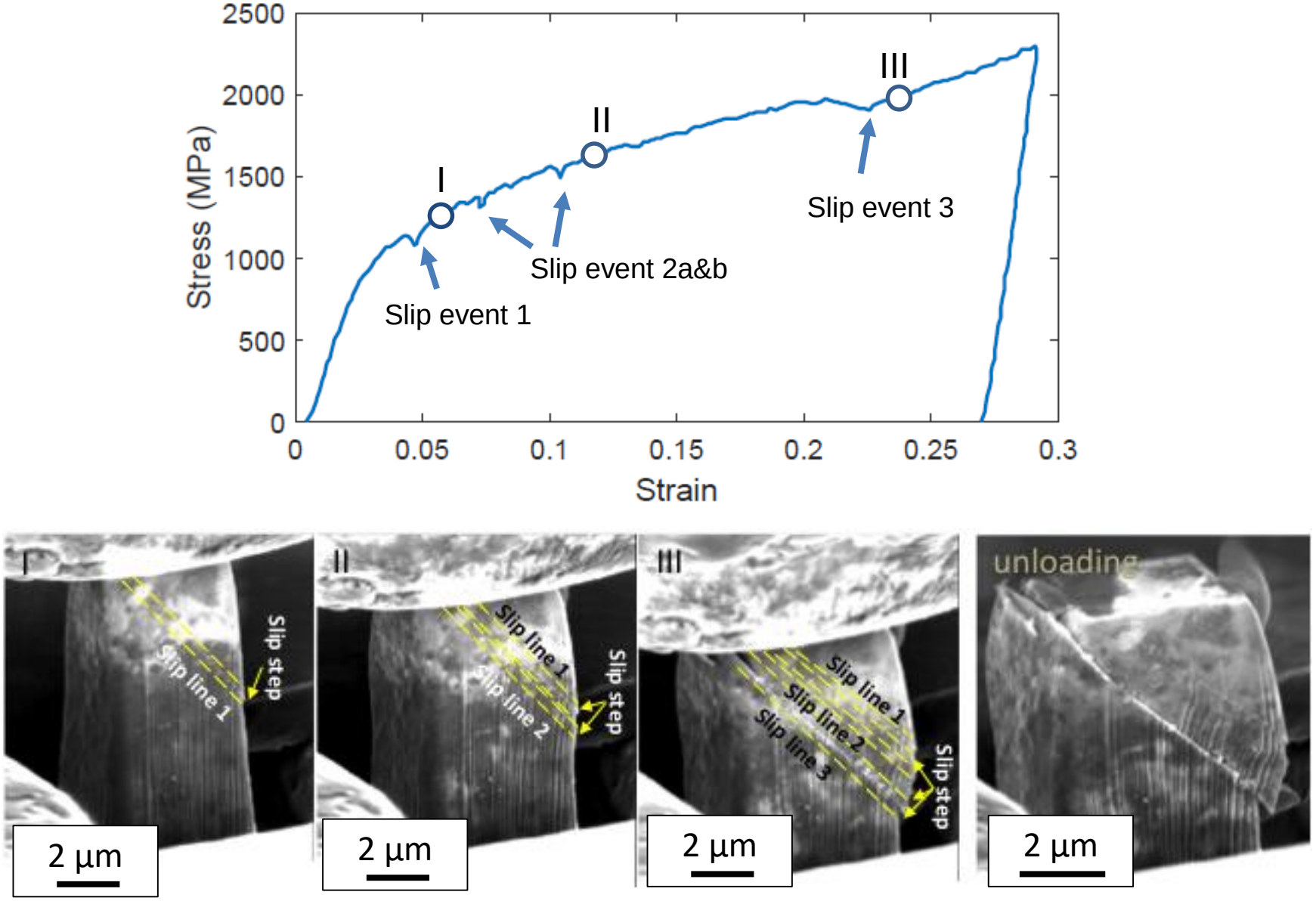


FIGURE 9. Engineering stress-strain curves for [001]-oriented square micropillars. Snapshots of the micropillar corresponding to strains of (I) 6 (II) 12% and (III) 25% highlighting slip activity following each load-drop event.

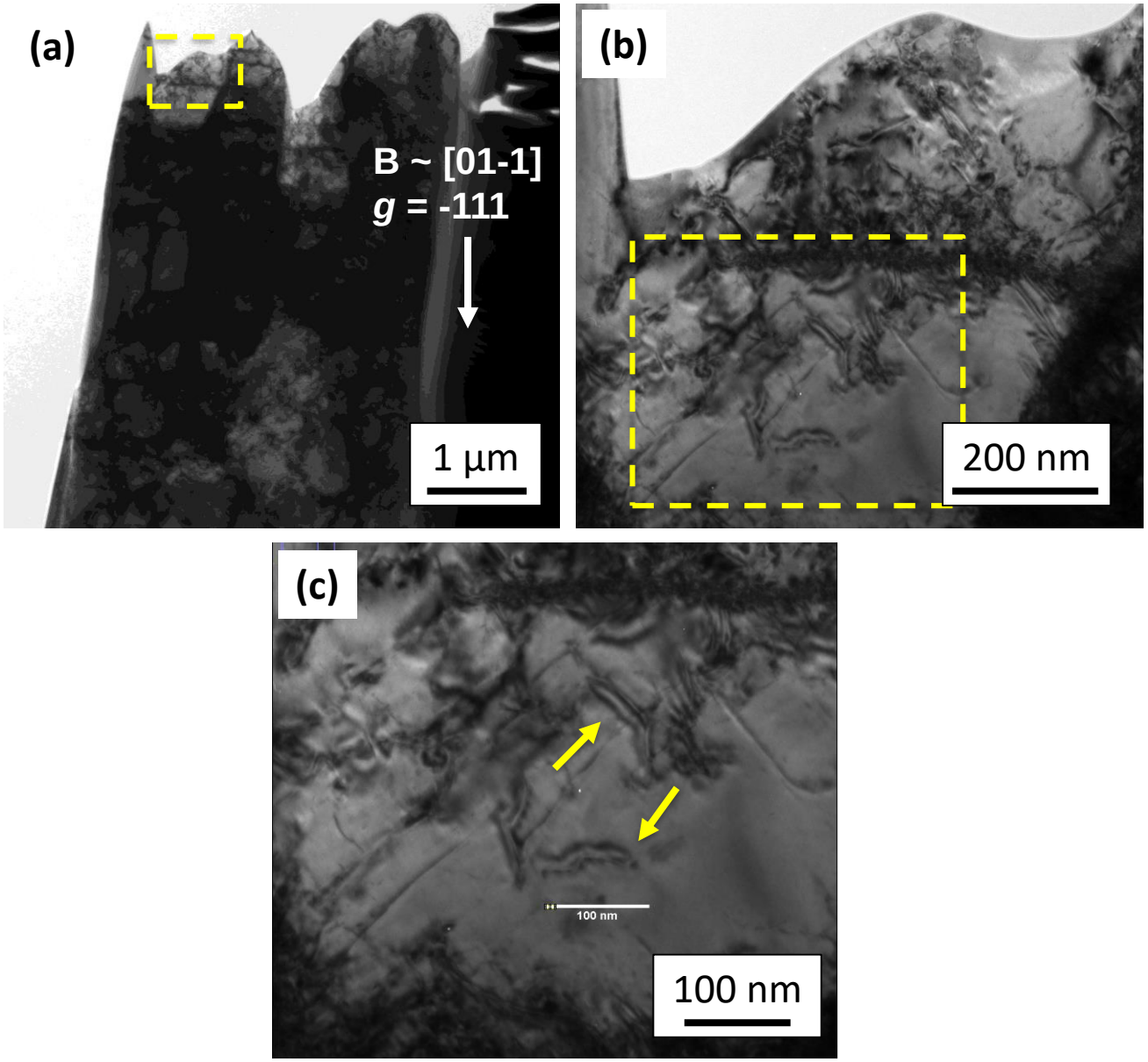


FIGURE 10. Bright field images showing a high strain contrast region in a foil, lifted out from a compressed

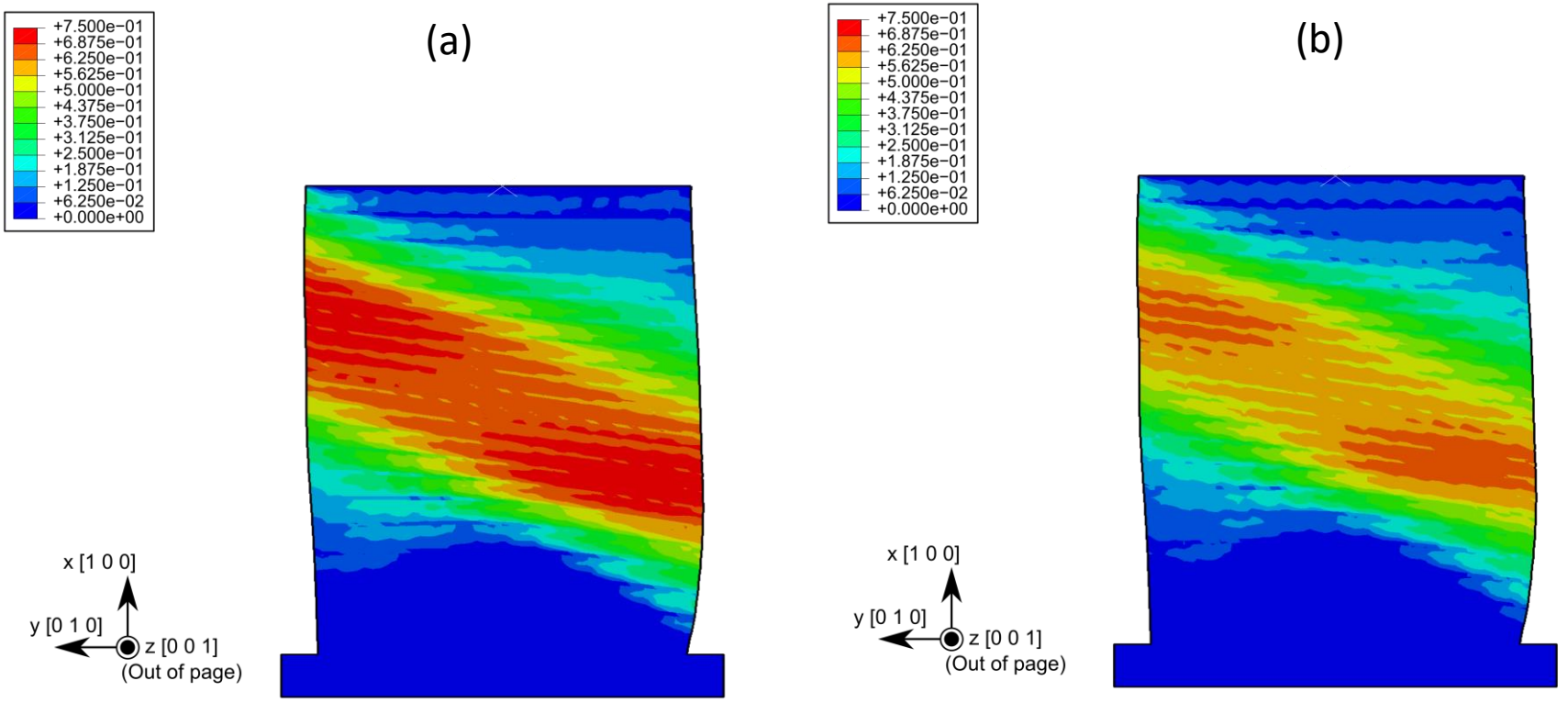


FIGURE 11. Crystal plasticity modeling of the near [100] micropillar showing the strain distribution on the two slip systems (a) (11-1) [101] and (b) (111) [-101] with highest Schmid factor for the given orientation.

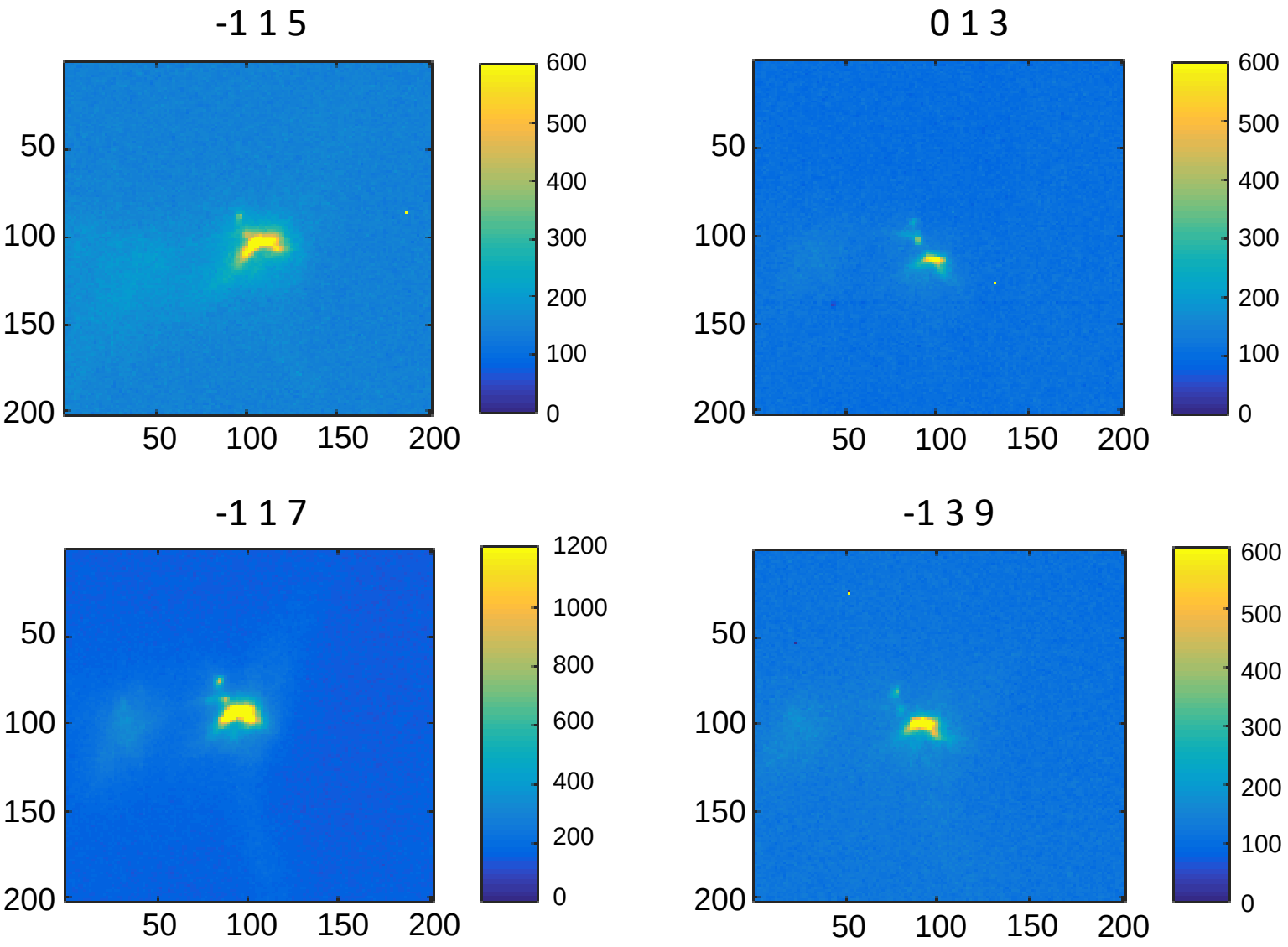


Supplementary FIGURE S1. Different peaks isolated from the whole Laue pattern obtained for the undeformed parent micropillar.

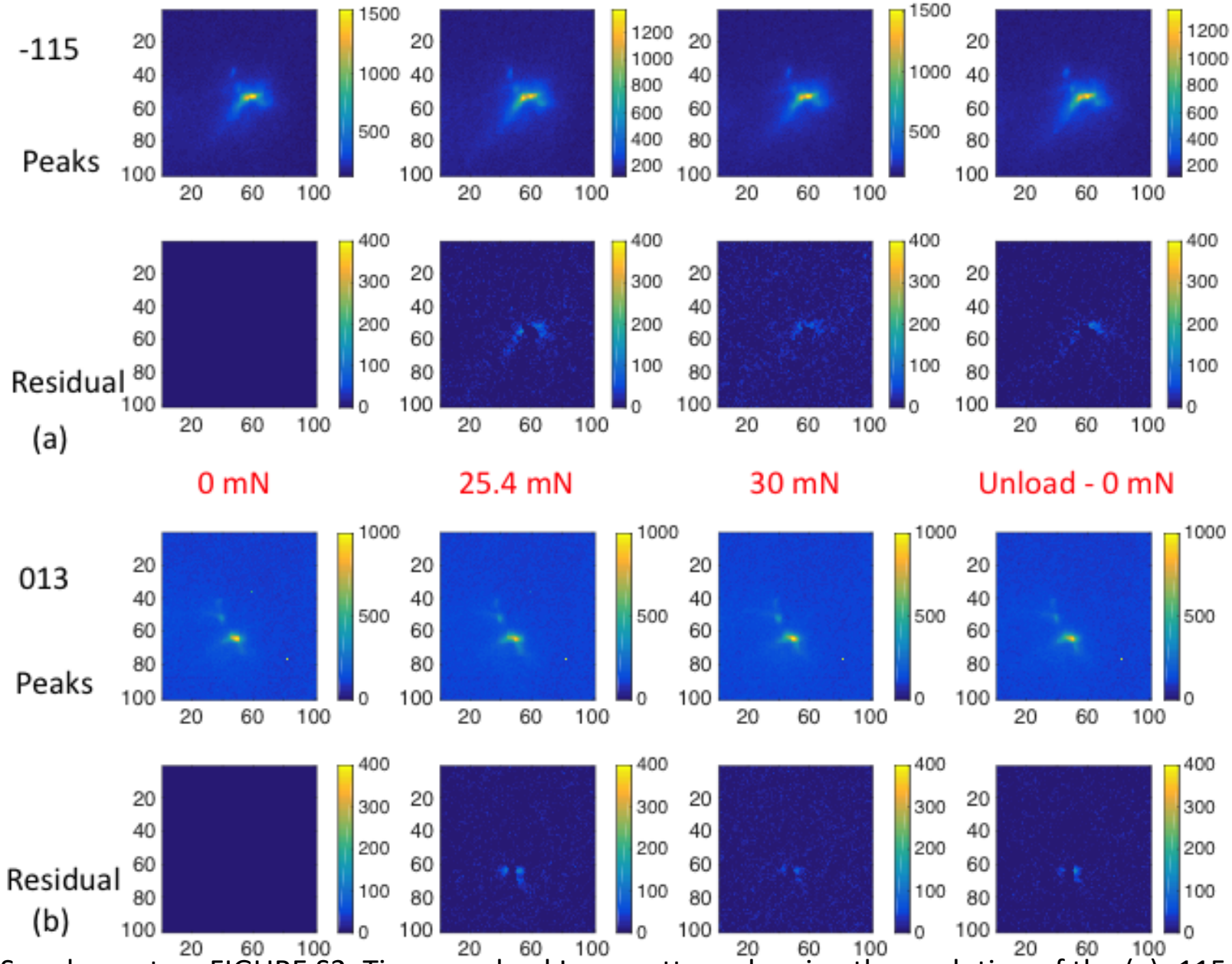


Supplementary FIGURE S2. Time-resolved Laue pattern showing the evolution of the (a) -115, (b) 013, (c) -117 and (d) -139 peaks during compression of the micropillar upto peak load till unloading. The corresponding residual plots are also shown.

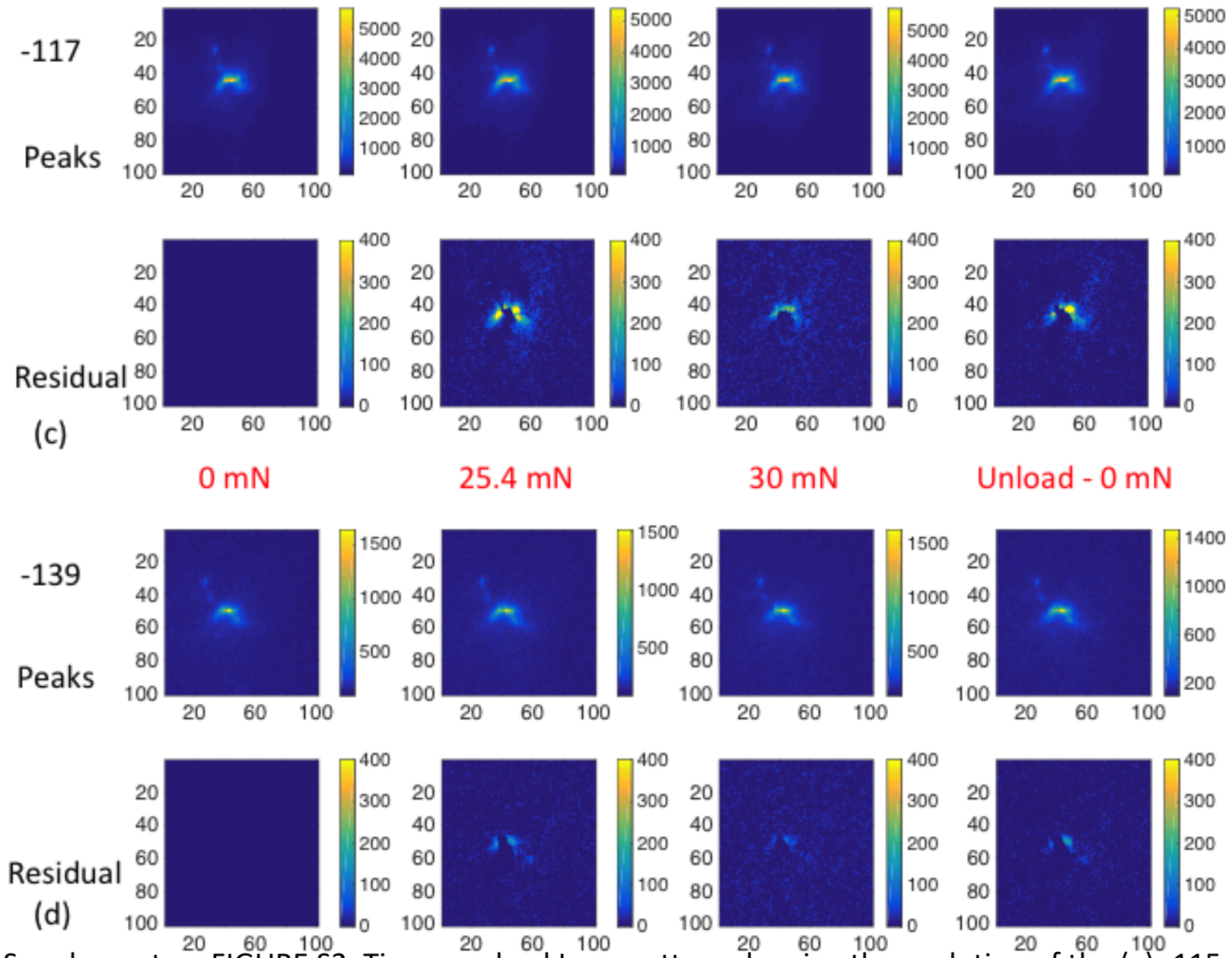


Supplementary FIGURE S2. Time-resolved Laue pattern showing the evolution of the (a) -115, (b) 013, (c) -117 and (d) -139 peaks during compression of the micropillar upto peak load till unloading. The corresponding residual plots are also shown.

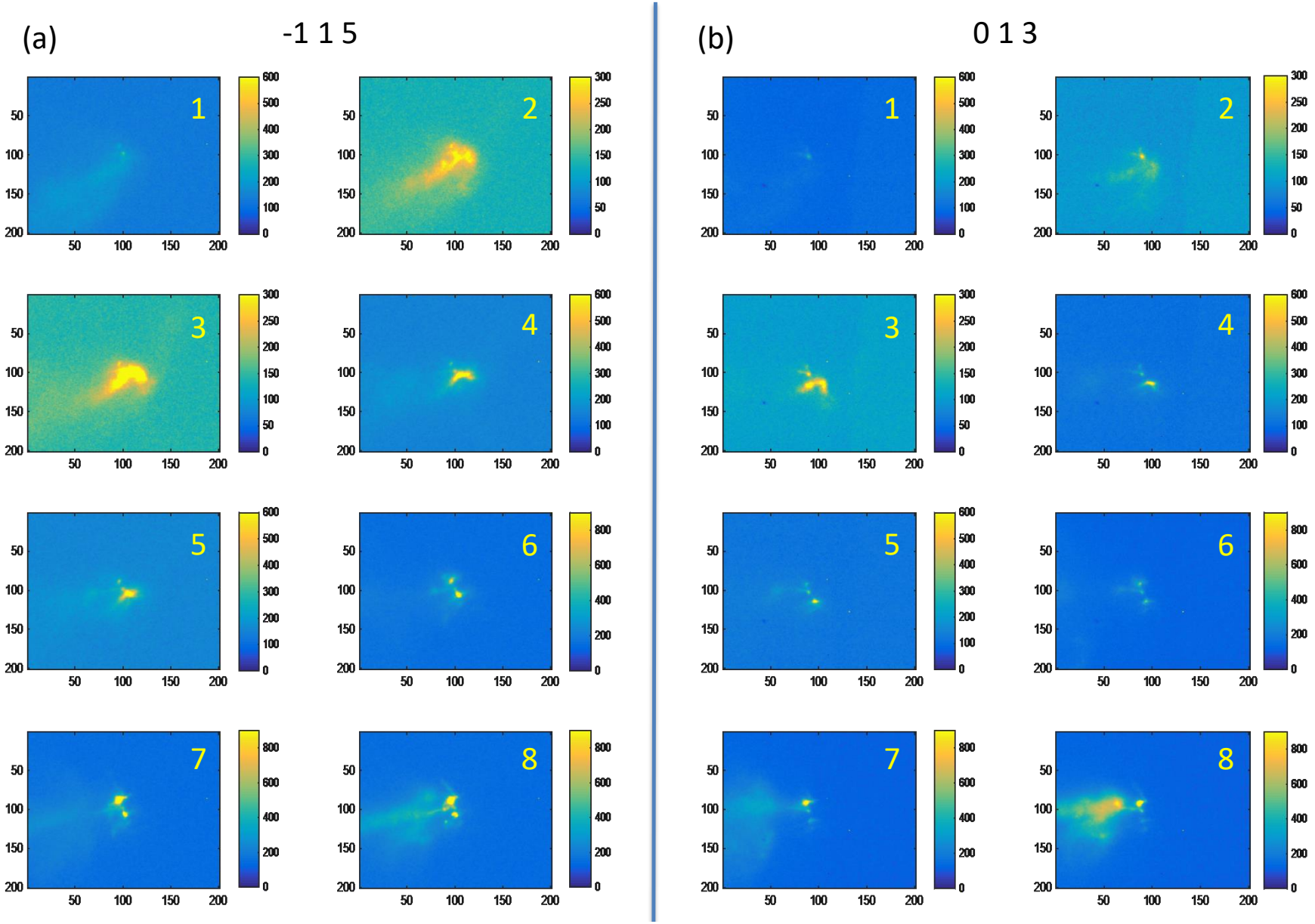


Supplementary FIGURE S3. MicroLaue patterns of (a) -115, (b) 013, (c) -117 and (d) -139 peaks obtained along the vertical axis of the compressed micropillar sample. The number on the patterns denote the positions on the micropillar as indicated in Figure 6.

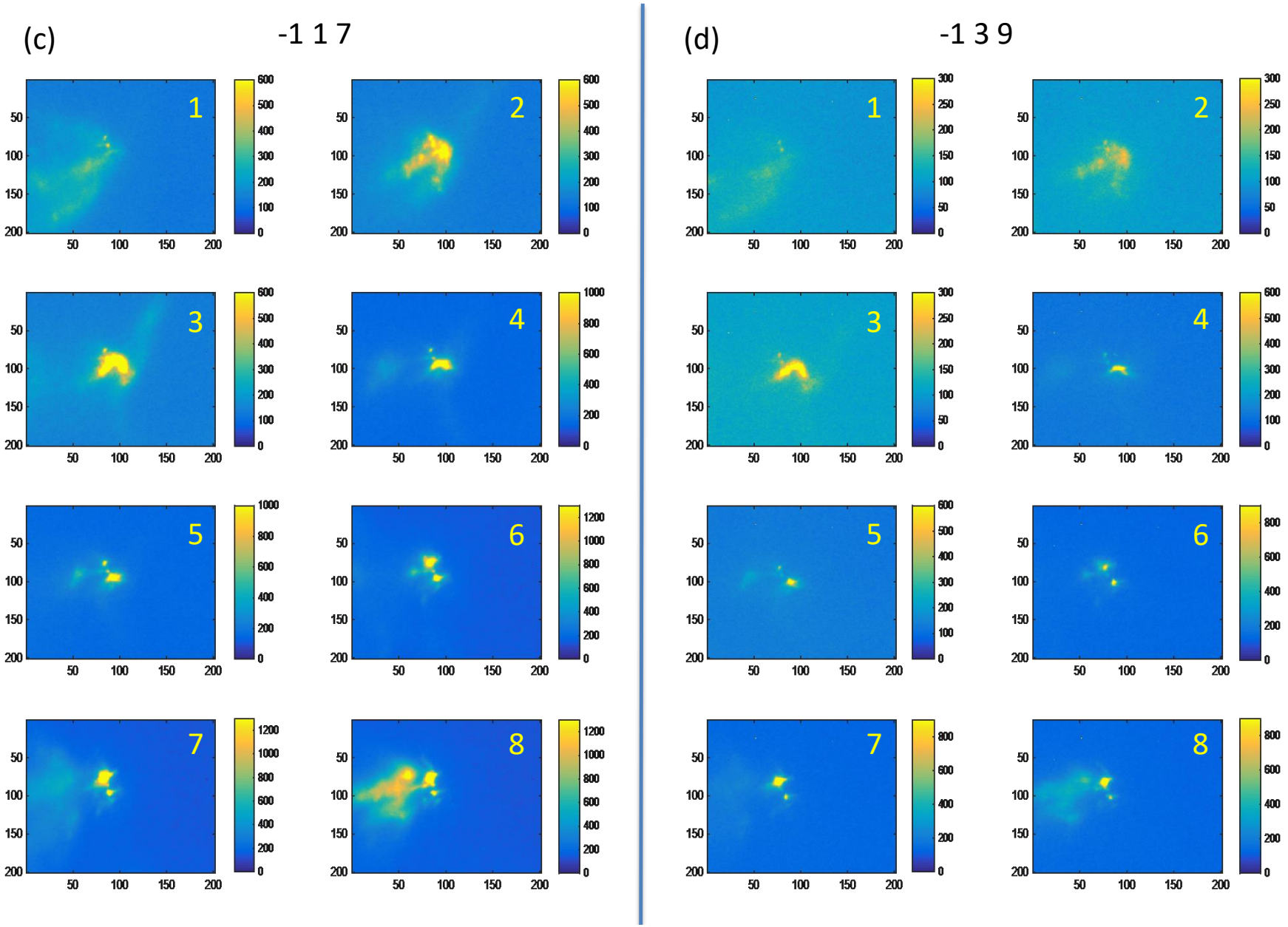


Supplementary FIGURE S3. MicroLaue patterns of (a) -115, (b) 013, (c) -117 and (d) -139 peaks obtained along the vertical axis of the compressed micropillar sample. The number on the patterns denote the positions on the micropillar as indicated in Figure 6.

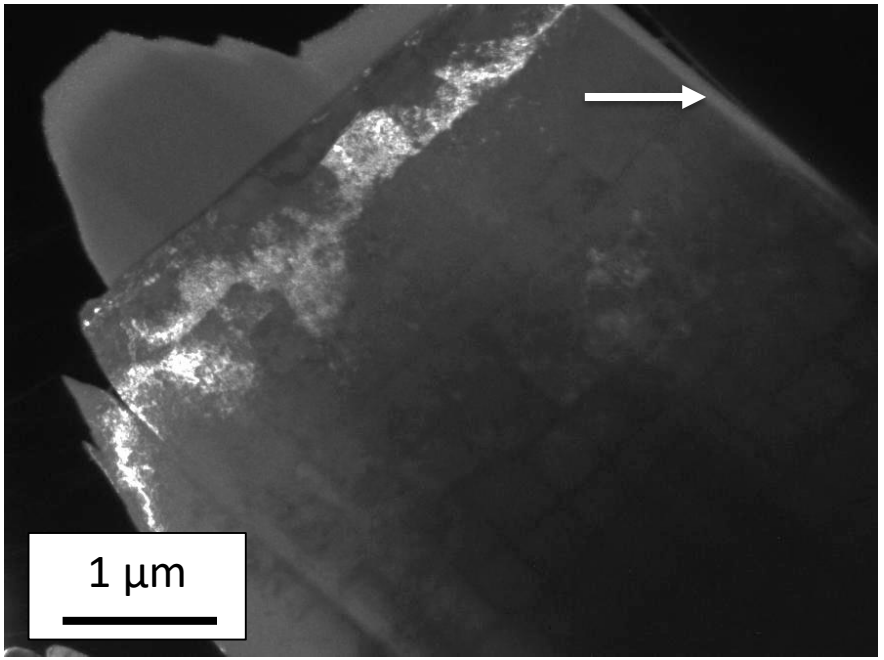


Supplementary FIGURE S4. Dark field image (taken with $\vec{g}$=202, white arrow) of the deformed micropillar showing the presence of a highly strained layer on the top of the pillar, caused due to friction between the pillar surface and punch, manifested as a distinct orientation.

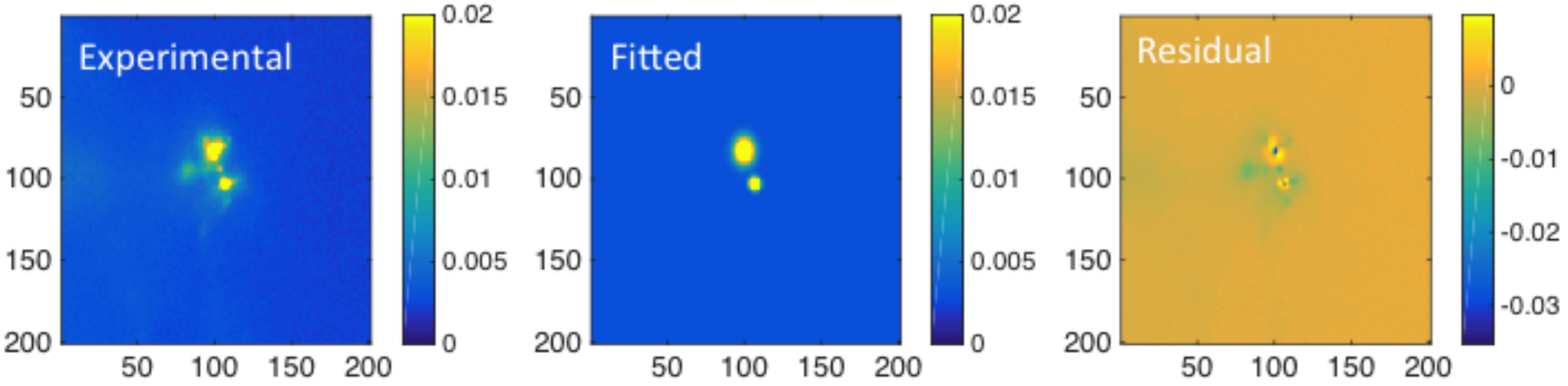


Supplementary FIGURE S5. An example of fitting two γ and γ’ peaks with individual Gaussian peak functions. This was done for all reflections along the length of the pillar post-deformation.

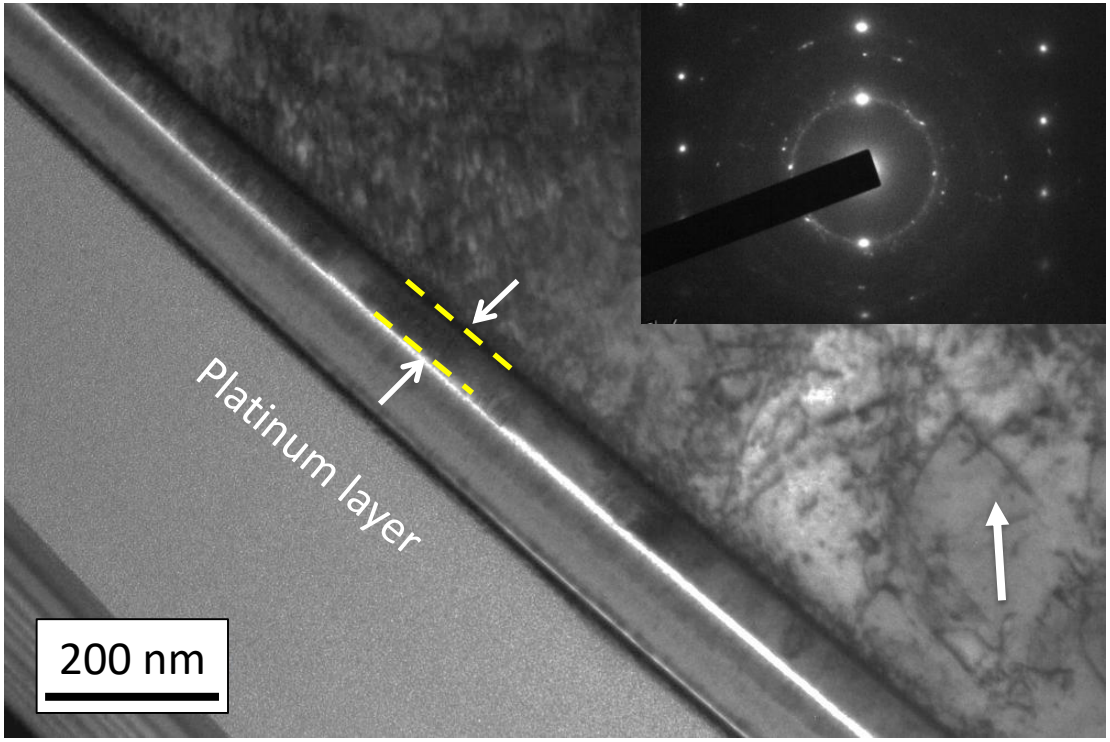


Supplementary FIGURE S6. TEM image of side of the sectioned parent micropillar showing the presence of an amorphous layer formed due to ion implantation during FIB milling of the pillar. The white arrow shows $\vec{g}$=202 vector.

(a)

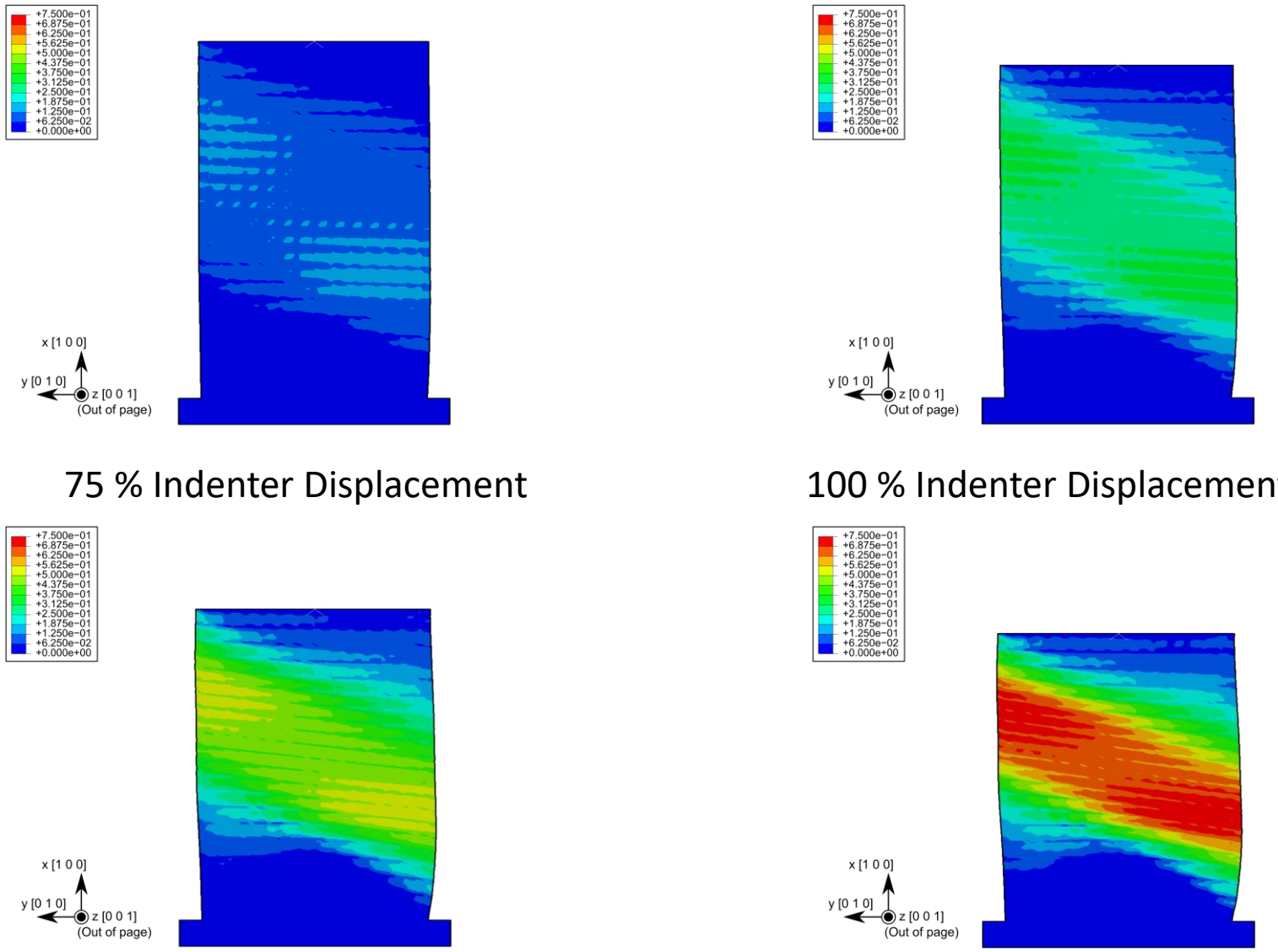


Figure S7. Crystal plasticity modeling of the near [100] micropillar showing the strain distribution on the two slip systems (a) (11-1) [101] and (b) (111) [-101] with highest Schmid factor for the given orientation at different stages of loading.

(b) 25 % Indenter Displacement

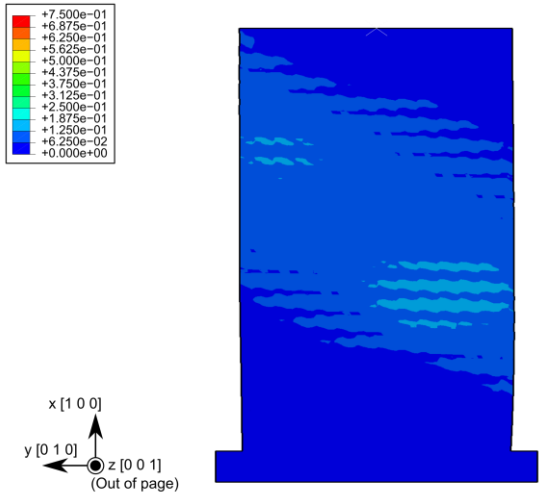


50 % Indenter Displacement

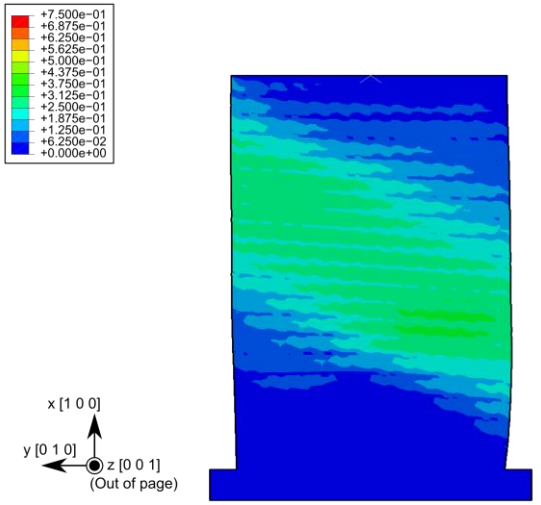


75 % Indenter Displacement

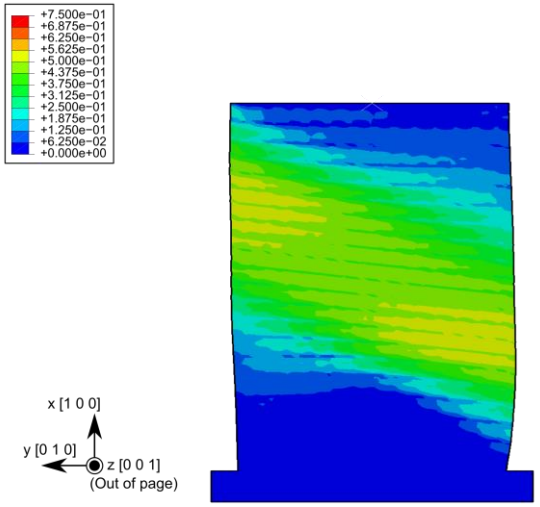


100 % Indenter Displacement

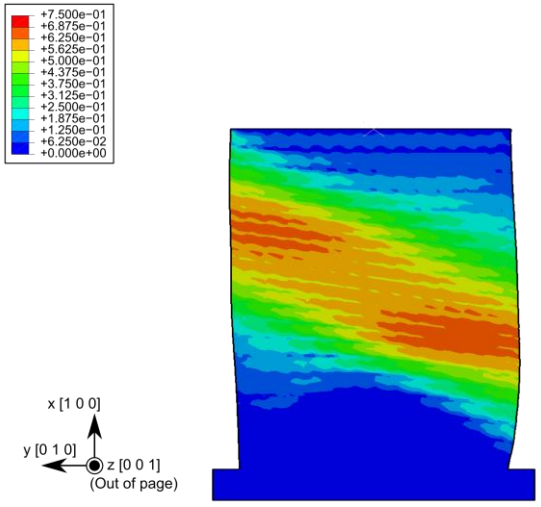


Figure S7. Crystal plasticity modeling of the near [100] micropillar showing the strain distribution on the two slip systems (a) (11-1) [101] and (b) (111) [-101] with highest Schmid factor for the given orientation at different stages of loading.